

國立交通大學

電信工程學系碩士班

碩士論文

IEEE 802.15.3c 多重載波高速介面系統之空間多重擷取

Spatial Division Multiple Access for IEEE 802.15.3c
Multicarrier HSI System

研究生：洪郁勳

指導教授：吳文榕 博士

中華民國九十八年七月

IEEE 802.15.3c 多重載波高速介面系統之空間多重擷取

Spatial Division Multiple Access for IEEE 802.15.3c

Multicarrier HSI System

研究生：洪郁勛

指導教授：吳文榕 教授

國立交通大學電信工程學系碩士班



IEEE 802.15.3c 為一在短距離傳送未經壓縮的高解析視訊、音訊及資料之規格。由於使用位於免執照的 60GHz 頻帶，因此在此頻帶中將遭受到嚴重的傳播損耗(propagation loss)。為了解決這項問題，利用平面天線陣列(planar antenna array)及波束形成技術(beamforming)是一個經常使用來補償遺失的方法。在本論文中，我們首先設計了 IEEE802.15.3c 之正交頻分複用技術(OFDM)接收器，並利用平面天線陣列實現空間分割多重存取(SDMA)，進而模擬 IEEE802.15.3c 之無線個人區域網路(PAN)。在 SDMA 中，各個方向之波束是同時產生的，然而各個波束之間所形成之干擾成為我們主要關心的問題。最近，一種結合數位權重與相位偏移器的混合式的天線陣列被提出來。利用這樣的架構之下，可有效的消除波束之間的干擾。我們利用多重輸入多重輸出(MIMO)系統來模擬 SDMA 系統，並計算比較 SDMA 使用類比波束形成(analog beamforming)與數位波束形成(digital beamforming)在 IEEE802.15.3c 之下的效能。

Spatial Division Multiple Access for IEEE 802.15.3c Multicarrier HSI System

Student : Yu-Hsun Hong Advisor : Dr. Wen-Rong Wu

Department of Communication Engineering

National Chiao-Tung University

Abstract

IEEE 802.15.3c is a high data-rate specification proposed to transfer uncompressed high-definition video, audio, and data in short distance. Since it operates in unlicensed 60GHz band, it endures a severe propagation loss. To solve the problem, a planar antenna array conducting beamforming is usually needed to compensate for the loss. In this thesis, we first design an OFDM receiver for the IEEE802.15.3c system. Then, we take advantage of the antenna array to propose a spatial division multiple access (SDMA) system for IEEE802.15.3c personal area network (PAN). In SDMA, multiple beams are formed simultaneously, and interference between these beams becomes the main concern. Recently, a hybrid array, which can conduct beamforming using digital weights and phase shifters, was proposed. With the architecture, interference cancellation becomes possible. We model a SDMA system with a multiple-input-multiple output (MIMO) system and evaluate the performance of an IEEE 802.15.3c SDMA system with analog and hybrid beamforming.

誌謝

首先，我要感謝我的指導教授吳文榕老師在這兩年來的諄諄教誨，引領我在通訊領域中自由自在的翱翔。老師的治學態度嚴謹，與學生相處卻又如慈父一般，不論在研究方面，在人生方面，都使我走向了一個全新的境界。我也要感謝實驗室的李俊芳學長、許兆元學長、曾凡碩學長、謝弘道學長、林鈞陶學長，他們在課業研究上對我更是不吝指導，猶如一盞明燈點亮了我每個苦思的夜。而碩士班一同打拚努力的呂珮聰，楊植纓與柯國仁三位同學，不時的關懷與支持，更是令我深懷感謝之意。另外要感謝伍紹勳教授與行動寬頻無線通訊實驗室的林科諺同學在研究上給予我的支援。最後，我要感謝我的家人在這兩年來的支持與鼓勵，我愛你們！



Contents

摘要.....	i
Abstract.....	ii
誌謝.....	iii
Contents.....	iv
List of figures.....	vi
List of tables.....	x
Chapter 1 Introduction.....	1
Chapter 2 IEEE 802.15.3C Specification Overview.....	4
2.1 Introduction.....	4
2.2 Preamble Structure.....	5
2.3 PHY Payload Field.....	7
2.3.1 Scrambler.....	7
2.3.2 HSI PHY FEC.....	8
2.3.2.1 LDPC Block Code.....	9
2.3.2.2 Bit Interleaver.....	11
2.3.3 Constellation Mapping.....	12
2.3.4 Spreader.....	14
2.3.5 Tone Interleaver.....	15
2.3.6 HIS PHY OFDM modulator.....	15
2.3.7 Pilot Subcarriers.....	16
2.3.8 Guard Subcarriers.....	17
Chapter 3 IEEE 802.15.3c Receiver Design.....	18
3.1 Inner Receiver Structure.....	18
3.2 Frame Detection.....	18

3.3 Frequency Synchronization.....	20
3.4 Symbol Timing.....	22
3.5 Channel Estimation.....	23
3.6 Phase Tracking.....	25
Chapter 4 Spatial Division Multiple Access in IEEE 802.15.3c Systems.....	28
4.1 Introduction.....	28
4.2 Architecture of Planar Antenna Array.....	30
4.3 The Array Pattern of Planar Antenna Arrays.....	30
4.4 MIMO Modeling of SDMA Systems.....	36
Chapter 5 MIMO Detectors in OFDM Systems.....	40
5.1 System Model.....	40
5.2 MIMO Detector.....	42
5.2.1 Zero Forcing and Minimum Mean-Square Error Detectors...42	
5.2.2 VBLAST Algorithm.....	43
5.2.3 Maximum Likelihood detector.....	44
Chapter 6 Simulations.....	47
Chapter 7 Conclusions.....	69
7.1 Conclusion.....	69
7.2 Future work.....	70
Reference.....	71

List of Figure

Figure 2-1 The transmitter block diagram of 802.15.3c HSI PHY.....	4
Figure 2-2 Realization of scrambling with PRBS generator.....	7
Figure 2-3 FEC process for HSI PHY.....	9
Figure 2-4-1 Parity check matrices of rate-1/2.....	10
Figure 2-4-2 Parity check matrices of rate-5/8.....	11
Figure 2-4-3 Parity check matrices of rate-3/4.....	11
Figure 2-4-4 Parity check matrices of rate-7/8.....	11
Figure 2-5 Bit interleaver structure.....	12
Figure 2-6 QPSK, 16-QAM, 64-QAM constellation bits encoding.....	13
Figure 2-7 Subcarrier frequency allocation.....	16
Figure 3-1 Signal flow structure of inner receiver.....	18
Figure 3-2 Signal flow structure of the delay and correlate algorithm.....	19
Figure 3-3 Preamble used for frame detect.....	20
Figure 3-4 Preamble used for frequency synchronization.....	21
Figure 3-5 Preamble used for symbol timing.....	23
Figure 3-6 Preamble used for channel estimation.....	24
Figure 3-7 Signal flow structure of phase compensator.....	26
Figure 4-1 Architecture of planar antenna arrays.....	29
Figure 4-2 Block diagram of Hybrid Beamforming.....	29
Figure 4-3 Configuration of planar antenna arrays.....	30
Figure 4-4 Initial structure of planar antenna arrays.....	33
Figure 4-5 Rearrange structure of planar antenna arrays.....	34
Figure 4-6 Planar antenna arrays of configuration 2 with two weights per user.....	35

Figure 4-7 Planar antenna arrays of configuration 2 with four weights per user.....	35
Figure 4-8 Beamforming pattern with two users (2 weights) between $\pi/2$	37
Figure 4-9 Beamforming pattern with two users (2 weights) between $3\pi/4$	37
Figure 4-10 Beamforming pattern with two users (4 weights) between $\pi/2$	38
Figure 4-11 Beamforming pattern with two users (4 weights) between $3\pi/4$	38
Figure 5-1 MIMO-OFDM transmitter block diagram.....	41
Figure 5-2 MIMO-OFDM receiver block diagram.....	42
Figure 6-1 BER comparison of LDPC iteration for coding rate 1/2 in QPSK AWGN channel.....	48
Figure 6-2 BER comparison of LDPC iteration for coding rate 3/4 in QPSK AWGN channel.....	49
Figure 6-3 BER comparison of LDPC iteration for coding rate 7/8 in QPSK AWGN channel.....	49
Figure 6-4 BER comparison of LDPC iteration for coding rate 1/2 in 16QAM AWGN channel.....	50
Figure 6-5 BER comparison of LDPC iteration for coding rate 3/4 in 16QAM AWGN channel.....	50
Figure 6-6 BER comparison of LDPC iteration for coding rate 7/8 in 16QAM AWGN channel.....	51
Figure 6-7 BER comparison of LDPC iteration for coding rate 5/8 in 64QAM AWGN channel.....	51
Figure 6-8 BER comparison of LDPC iteration for coding rate 1/2 in QPSK multipath Rayleigh fading channel.....	52
Figure 6-9 BER comparison of LDPC iteration for coding rate 3/4 in QPSK multipath Rayleigh fading channel.....	52
Figure 6-10 BER comparison of LDPC iteration for coding rate 7/8 in QPSK	

multipath Rayleigh fading channel.....	53
Figure 6-11 BER comparison of LDPC iteration for coding rate 1/2 in 16QAM	
multipath Rayleigh fading channel.....	53
Figure 6-12 BER comparison of LDPC iteration for coding rate 3/4 in 16QAM	
multipath Rayleigh fading channel.....	54
Figure 6-13 BER comparison of LDPC iteration for coding rate 7/8 in 16QAM	
multipath Rayleigh fading channel.....	54
Figure 6-14 BER comparison of LDPC iteration for coding rate 5/8 in 64QAM	
multipath Rayleigh fading channel.....	55
Figure 6-15 Comparison of ideal and real-world condition for coding rate 1/2 in	
QPSK multipath Rayleigh fading channel.....	56
Figure 6-16 Comparison of ideal and real-world condition for coding rate 3/4 in	
QPSK multipath Rayleigh fading channel.....	56
Figure 6-17 Comparison of ideal and real-world condition for coding rate 7/8 in	
QPSK multipath Rayleigh fading channel.....	57
Figure 6-18 Comparison of ideal and real-world condition for coding rate 1/2 in	
16QAM multipath Rayleigh fading channel.....	57
Figure 6-19 Comparison of ideal and real-world condition for coding rate 3/4 in	
16QAM multipath Rayleigh fading channel.....	58
Figure 6-20 Comparison of ideal and real-world condition for coding rate 7/8 in	
16QAM multipath Rayleigh fading channel.....	58
Figure 6-21 Comparison of ideal and real-world condition for coding rate 5/8 in	
64QAM multipath Rayleigh fading channel.....	59
Figure 6-22 Analog beam pattern I.....	60
Figure 6-23 Digital beam pattern I.....	60

Figure 6-24 Hybrid beam pattern I.....	60
Figure 6-25 Analog beam pattern II.....	61
Figure 6-26 Digital beam pattern II.....	61
Figure 6-27 Hybrid beam pattern II.....	61
Figure 6-28 Performance of SDMA system with analog beamforming using ML detector (IEEE 802.15.3c).....	62
Figure 6-29 Performance of SDMA system with analog beamforming using VBLAST MMSE detector (IEEE 802.15.3c).....	63
Figure 6-30 Performance of SDMA system with analog beamforming using VBLAST ZF detector (IEEE802.15.3c).....	63
Figure 6-31 Performance of SDMA system with analog beamforming using MMSE detector (IEEE 802.15.3c).....	64
Figure 6-32 Performance of SDMA system with analog beamforming using ZF detector (IEEE 802.15.3c).....	64
Figure 6-33 Performance of analog beamforming comparison with angle 90°.....	65
Figure 6-34 Performance of analog beamforming comparison with angle 60°.....	66
Figure 6-35 Performance of analog beamforming comparison with angle 15°.....	66
Figure 6-36 Performance of analog beamforming comparison with angle 10°.....	67
Figure 6-37 Performance of analog beamforming comparison with angle 5°.....	67
Figure 6-38 Performance of SDMA system with hybrid beamforming using ML detector (IEEE 802.15.3c).....	69

List of Table

Table 2-1 HSI PHY preamble structure.....	5
Table 2-2 Length 128 Golay sequence c_{128} in hexadecimal notation.....	6
Table 2-3 Length 128 Golay sequence d_{128} in hexadecimal notation.....	6
Table 2-4 LDPC parameters.....	9
Table 2-5 Modulation dependent normalization factor.....	14
Table 2-6 Subcarrier frequency allocation.....	16
Table 6-1 HSI PHY MCS dependent parameters.....	47
Table 6-2 Power gain with different angles using analog beamforming.....	62
Table 6-3 Power gain with different angles using hybrid beamforming.....	68



Chapter 1 Introduction

With the increasing use of mobile devices in daily life, wireless communication of personal area network (WPAN) becomes more and more important in recent years. Because of the increasing demands for high-quality video applications, IEEE 802.15 WPAN Task Group (TG3c) formed in March 2005 has been developing a millimeter wave alternative physical layer (PHY) for WPAN. The millimeter wave WPAN can operate on the unlicensed band including 57 to 64 GHz. The characteristics of the high penetration loss and strong oxygen adsorption make the radio in 57 to 64 GHz band suitable for short distance transmission. The millimeter wave WPAN also allows coexistence with all other microwave systems defined in the IEEE 802.15 of WPANs. Additionally, it can support high data rate at least 1 Gbps applications such as the high speed internet access or video streaming.

This specification defines two modulation schemes, single-carrier and multicarrier. The multicarrier scheme exploits the orthogonal frequency division multiplexing (OFDM). The OFDM has been shown to be a promising technique and has been used in several wideband digital communication systems, such as the IEEE 802.11 wireless local area network (WLAN), the IEEE 802.16e Worldwide Interoperability for Microwave Access (WiMAX) Wireless MANs and terrestrial digital video broadcasting (DVB-T). The most important advantage of OFDM is that it has the ability to convert the multi-path frequency-selective fading channel into a band of flat fading sub-channels. The receiver can then easily conduct signal recovery with a simple equalization method. Also, OFDM symbols can also be generated by the efficient Fast Fourier transform (FFT) algorithm facilitating its real-world in implementation.

As mentioned, the propagation loss in 60GHz environments is severe. As a result, the antenna array, which can conduct transmit/receive beamforming, is usually equipped in a transceiver. In the IEEE802.15.3c, a PAN is defined in which a user can only communicate with another. With multiple antennas in the transmitter/receiver, however, we can have more advanced applications, e.g, the spatial division multiple access (SDMA). In SDMA, a user can communicate with multiple users simultaneously. In other words, a transmitter/receiver can form multiple beams pointing to multiple directions. As long as the interference between these beams can be controlled under a level, reliable communication between the links can be achieved.

In this thesis, we first design an OFDM receiver for the IEEE802.15.3c system. Then, we propose a SDMA system for IEEE802.15.3c WPAN. For beamforming, a planar antenna arrays with phase shifters for each antenna element is commonly used. Since the phase shift can only adjust the phase of the input signal analog, it cannot conduct interference cancellation. Recently, a hybrid array, which can conduct beamforming using digital weights and phase shifters, was proposed [7]. With the architecture, interference cancellation becomes possible. We will evaluate the performance of an IEEE 802.15.3c SDMA system with analog and hybrid beamforming. Since multiple bit streams are transmitted/received simultaneously in a SDMA system, it can be modeled as a multi-input multi-output (MIMO) system which is also referred to as a multiuser MIMO system. We will use a simple method to provide the modeling.

The rest of this thesis is organized as follow: In Chapter 2, we present the specification of 802.15.3c D04, which include the transmitter structure, preamble structure, and system parameters. In Chapter 3, we design the receiver structure constructing synchronization and channel estimation. In Chapter 4, we briefly review

the hybrid beamforming in [6] and establish the MIMO model for SDMA. In Chapter 5, we describe some commonly used MIMO detection algorithms. In the Chapter 6, we show the simulation result and performance comparison. Finally, we draw conclusions in Chapter 7.



Chapter 2 IEEE 802.15.3C Specification Overview [1]

2.1 Introduction

IEEE 802.15.3c is a physical layer specification for high rate wireless personal area networks (WPANs). In this chapter, we will focus on High Speed Interface mode of mmWave PHY (HSI PHY). It is designed for devices with low-latency, bidirectional high-speed data and orthogonal frequency domain multiplexing (OFDM) is used as the modulation scheme. HSI PHY supports a variety of modulation and coding schemes (MCSs) using different frequency-domain spreading factors, modulations, and low density parity check (LDPC) block codes. Figure 2-1 shows the transmitter block diagram given in the specification.

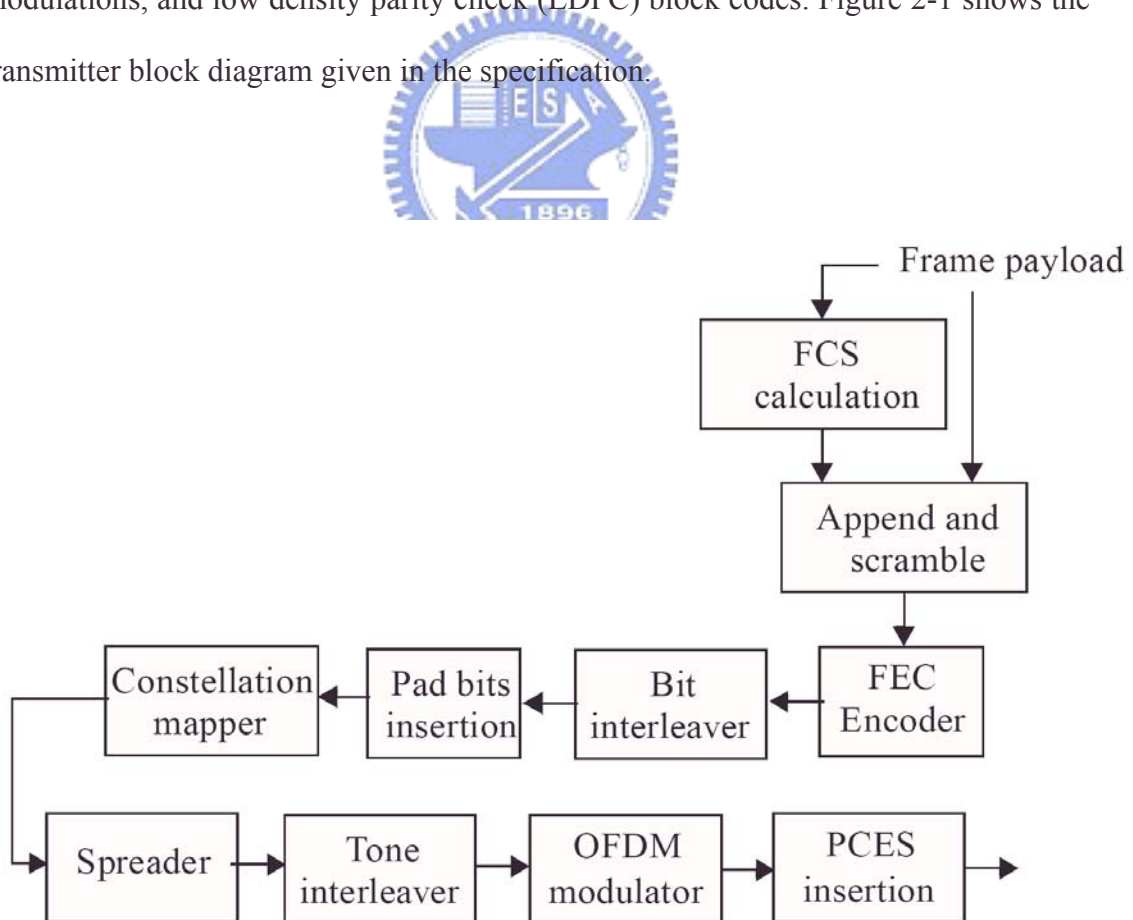


Figure 2-1 The transmitter block diagram of 802.15.3c HSI PHY

2.2 Preamble structure

A PHY preamble, which is given in Table 2-1, shall be added prior to the frame header to aid receiver operations related to frame detection, auto gain control(AGC) setting, timing acquisition, frequency recovery, frame synchronization, and channel estimation. The PHY preamble shall be transmitted at the rate of $R_S = 5.0625\text{M}$ samples/s. A preamble symbol is defined as a sequence of length 512 chips which corresponds to the FFT length.

There are defined three different preambles, the mandatory long preamble, mandatory medium preamble, and optional short preamble. All fields of the preambles are based on length 128 complementary Golay sequences \mathbf{c}_{128} and \mathbf{d}_{128} , which are given in Table 2-2 and Table 2-3 respectively.



	CES	SFD	SYNC
Long preamble:	$\bar{\mathbf{d}}_{128} \mathbf{p}_{512} \mathbf{p}_{512} \mathbf{p}_{512} \mathbf{p}_{512} \mathbf{p}_{512} \mathbf{p}_{512} \mathbf{p}_{512} \mathbf{p}_{512} \mathbf{p}_{512}$	$\mathbf{p}_{512} \mathbf{p}_{512} \bar{\mathbf{p}}_{512} \mathbf{p}_{512}$	\mathbf{c}_{128} (128 repetitions)
Medium preamble:	$\bar{\mathbf{d}}_{128} \mathbf{p}_{512} \mathbf{p}_{512} \mathbf{p}_{512} \mathbf{p}_{512}$	\mathbf{q}_{512}	\mathbf{c}_{128} (16 repetitions)
Short preamble:	$\bar{\mathbf{d}}_{128} \mathbf{p}_{512} \mathbf{p}_{512}$	\mathbf{p}_{512}	\mathbf{c}_{128} (16 repetitions)

Table 2-1 HSI PHY preamble structure

Code name	Value
Re[c_{128}]	509CC905AF9C3605AF6336FAAF9C3605
Im[c_{128}]	FA3663AF05369CAF05C99C5005369CAF

Table 2-2 Length 128 Golay sequence c_{128} in hexadecimal notation

Code name	Value
Re[d_{128}]	5F93C60AA093390AA06C39F5A093390A
Im[d_{128}]	F5396CA00A3993A00AC6935F0A3993A0

Table 2-3 Length 128 Golay sequence d_{128} in hexadecimal notation

Packet synchronization (SYNC) field :

The first field of preamble is used for frame detection, AGC setting, and timing acquisition. The SYNC field in the long preamble is obtained by repeating c_{128} 128 times, and that in the medium and short preamble is obtained by repeating c_{128} 16 times.

Packet start frame delimiter (SFD) :

The second field of the preamble, SFD, is provided to establish frame timing, in which length 512 Golay sequences p_{512} or q_{512} are used. Sequences p_{512} or q_{512} are constructed from c_{128} and d_{128} using the following equations.

$$p_{512} = [c_{128} \overline{d_{128}} \overline{c_{128}} \overline{d_{128}}] \quad (2-1)$$

$$q_{512} = [\overline{c_{128}} d_{128} \overline{c_{128}} \overline{d_{128}}] \quad (2-2)$$

where \bar{x} denote the complement sequence of x . The long preamble uses the sequence $[p_{512} p_{512} \bar{p}_{512} p_{512}]$ whereas the medium preamble uses only $[q_{512}]$ and the short preamble uses $[p_{512}]$ in field SFD.

Channel estimation sequence (CES) :

The third field of preamble, which is used to conduct channel estimation, repeats p_{512} 8 times and appends the result to \bar{d}_{128} to construct CES in the long preamble. In medium and short preambles, \bar{d}_{128} is appended to 4 and 2 repetitions of p_{512} respectively.

2.3 PHY pay load field

2.3.1 Scrambler



The frames shall be scrambled by a pseudo-random-bit-stream (PRBS) sequence

using a modulo-2 addition, as illustrated below:

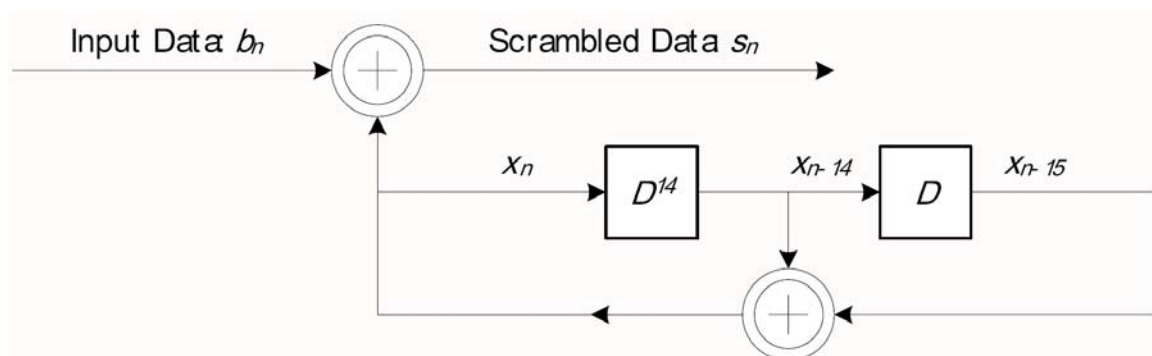


Figure 2-2 Realization of scrambling with PRBS generator

The polynomial for the PRBS generator used by the scrambler is:

$$g(D) = 1 + D^{14} + D^{15} \quad (2-3)$$

where D is a single bit delay element. The polynomial is a primitive polynomial and it can generate a maximal length sequence, By the given generator polynomial, the corresponding PRBS, is generated as:

$$x_n = x_{n-14} \oplus x_{n-15}, \quad n = 0, 1, 2, \dots \quad (2-4)$$

The following sequence defines the initialization sequence:

$$\begin{aligned} x_{init} &= [x_{-1} x_{-2} x_{-3} x_{-4} x_{-5} x_{-6} x_{-7} x_{-8} x_{-9} x_{-10} x_{-11} x_{-12} x_{-13} x_{-14} x_{-15}] \\ &= [11010000101 S1 S2 S3 S4] \end{aligned} \quad (2-5)$$

The seed identifier value [S1 S2 S3 S4] is set to 0000, and the first 16 bits will be:

$$[x_1 x_2 x_3 \dots x_{15}] = [0001111000111010] \quad (2-6)$$

The scrambled data bits, s_n , are obtained as follows:

$$s_n = b_n \oplus x_n \quad (2-7)$$

where b_n represents the unscrambled data bits. The side-stream de-scrambler at the receiver shall be initialized with the same initialization vector, x_{init} , used in the transmitter scrambler.

2.3.2 HSI PHY FEC

The forward error control coding (FEC) process is illustrated as follow

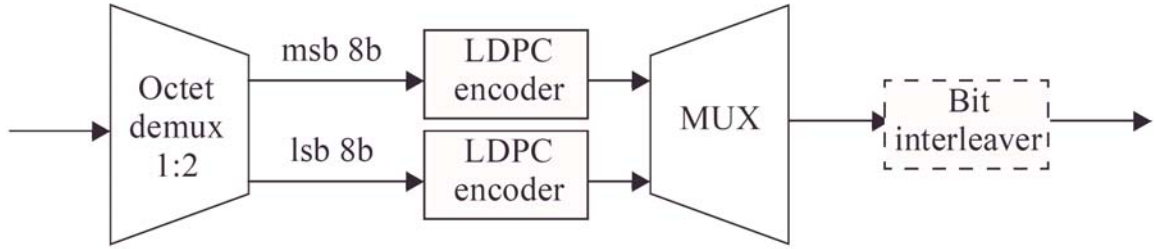


Figure 2-3 FEC process for HSI PHY

2.3.2.1 LDPC block code

The supported LDPC block FEC rates, information block lengths, L_{INF} , and codeword block lengths, L_{FEC} , are described in Table 2-4

R_{FEC}	L_{INF} (bits)	L_{FEC} (bits)
1/2	336	672
5/8	420	
3/4	504	
7/8	588	


Table 2-4 LDPC parameters

The LDPC encoder is systematic, it encodes an information block of size k , $i = (i_0, i_1, \dots, i_{(k-1)})$, into a codeword c of size n , $c = (i_0, i_1, \dots, i_{(k-1)}, p_0, p_1, \dots, p_{(n-k-1)})$, by adding $n-k$ parity bits obtained so that $Hc^T = 0$, where H is an $(n - k) \times n$ parity check matrix.

Each of the parity-check matrices can be partitioned into square subblocks (submatrices) of size $z \times z$ ($z = 21$). These submatrices are either cyclic-permutations of the identity matrix or null (all-zero) submatrices. The cyclic-permutation matrix p^i is obtained from the $z \times z$ identity matrix by cyclically shifting the columns to the right by i elements. An example is showed below, the matrix p^0 is the $z \times z$ identity matrix, and matrix p^1 and p^2 are produced by cyclically shifting the columns of the identity matrix $I_{21 \times 21}$ to the right by 1 and 2 places, respectively.

$$p^0 = \begin{bmatrix} 1 & 0 & \dots & \dots & 0 \\ 0 & 1 & 0 & \dots & 0 \\ \dots & 0 & \ddots & 0 & \dots \\ 0 & \dots & 0 & 1 & 0 \\ 0 & \dots & \dots & 0 & 1 \end{bmatrix}, \quad p^1 = \begin{bmatrix} 0 & \dots & \dots & 0 & 1 \\ 1 & 0 & \dots & \dots & 0 \\ 0 & 1 & \ddots & 0 & 0 \\ \vdots & 0 & \ddots & 0 & \dots \\ 0 & \dots & 0 & 1 & 0 \end{bmatrix}, \quad p^2 = \begin{bmatrix} 0 & \dots & 0 & 1 & 0 \\ 0 & \dots & \dots & 0 & 1 \\ 1 & 0 & \dots & 0 & 0 \\ 0 & \ddots & 0 & \dots & \dots \\ 0 & 0 & 1 & 0 & 0 \end{bmatrix} \quad (2-8)$$

The LDPC encoder supports rate-1/2, rate-5/8, rate-3/4, and rate-7/8 encoding. Figure 2-4 displays the matrix permutation indices of parity-check matrices for all four FEC rates at block length $n = 672$ bits. The integer i denotes the cyclic-permutation matrix p^i . The ‘-’ entries in the table denote null (all zero) submatrices.



(672,336), Code rate: 1/2																																
	1	2	3	4	5	6	7	8	9	10	11	12	13	14	15	16	17	18	19	20	21	22	23	24	25	26	27	28	29	30	31	32
1	-	-	-	5	-	18	-	-	-	-	3	-	10	-	-	-	-	-	-	5	-	-	-	-	-	-	-	-	-	-	-	-
2	0	-	-	-	-	-	16	-	-	-	-	6	-	-	-	0	-	7	-	-	-	-	-	-	-	-	-	-	-	-	-	-
3	-	-	6	-	7	-	-	-	-	2	-	-	-	-	9	-	20	-	-	-	-	-	-	-	-	-	-	-	-	-	-	-
4	-	18	-	-	-	-	-	0	10	-	-	-	-	16	-	-	-	-	9	-	-	-	-	-	-	-	-	-	-	-	-	-
5	5	-	-	-	-	-	18	-	-	-	-	3	-	10	-	-	5	-	-	-	-	-	-	4	5	-	-	-	-	-	-	-
6	-	0	-	-	-	-	-	16	6	-	-	-	0	-	-	-	-	-	7	-	4	-	-	-	-	-	10	-	-	-	-	-
7	-	-	-	6	-	7	-	-	-	-	2	-	-	-	-	9	-	20	-	-	-	4	-	-	-	-	-	19	-	-	-	-
8	-	-	18	-	0	-	-	-	-	10	-	-	-	-	16	-	-	-	-	9	-	-	12	-	-	4	-	-	-	-	-	-
9	-	5	-	-	-	-	-	18	3	-	-	-	-	-	10	-	-	5	-	-	4	-	-	-	-	-	-	-	-	-	-	-
10	-	-	0	-	16	-	-	-	-	6	-	-	-	0	-	-	-	-	-	7	-	4	-	-	-	-	-	-	-	-	-	-
11	6	-	-	-	-	-	7	-	-	-	-	2	9	-	-	-	-	-	-	20	-	-	-	4	-	-	-	-	-	-	-	-
12	-	-	-	18	-	0	-	-	-	-	10	-	-	-	-	16	9	-	-	-	-	-	-	12	-	-	-	-	-	-	-	-
13	-	-	5	-	18	-	-	-	-	3	-	-	-	-	10	-	-	5	-	-	4	-	-	-	-	-	5	-	7	-	-	-
14	-	-	-	0	-	16	-	-	-	-	6	-	-	-	0	-	7	-	-	-	-	4	-	10	-	-	-	-	-	-	19	-
15	-	6	-	-	-	-	-	7	2	-	-	-	-	9	-	-	-	-	-	20	-	-	-	4	-	19	-	-	-	-	-	10
16	18	-	-	-	-	-	0	-	-	-	-	10	16	-	-	-	-	9	-	-	12	-	-	-	-	-	-	4	-	17	-	-

Figure 2-4-1 Parity check matrices of rate-1/2

	1	2	3	4	5	6	7	8	9	10	11	12	13	14	15	16	17	18	19	20	21	22	23	24	25	26	27	28	29	30	31	32
1	0	-	-	5	-	18	16	-	-	-	3	6	10	-	-	0	-	7	-	5	-	-	4	4	-	10	-	5	-	7	-	19
2	-	-	6	-	7	-	-	-	-	2	-	-	-	-	9	-	20	-	-	-	4	-	-	-	-	-	19	-	10	-	-	-
3	-	18	-	-	-	-	-	0	10	-	-	-	-	16	-	-	-	-	9	-	-	12	-	-	4	-	-	-	-	-	17	-
4	5	0	-	-	-	-	18	16	6	-	-	3	0	10	-	-	5	-	7	-	4	-	-	4	5	-	10	-	19	-	7	-
5	-	-	-	6	-	7	-	-	-	-	2	-	-	-	-	9	-	20	-	-	-	4	-	-	-	-	-	19	-	10	-	-
6	-	-	18	-	0	-	-	-	-	10	-	-	-	-	16	-	-	-	-	9	-	-	12	-	-	4	-	-	-	-	-	17
7	-	5	0	-	16	-	-	18	3	6	-	-	-	0	10	-	-	5	-	7	4	4	-	-	-	5	-	10	-	19	-	7
8	6	-	-	-	-	-	7	-	-	-	-	2	9	-	-	-	-	-	20	-	-	-	4	-	19	-	-	-	-	-	10	-
9	-	-	-	18	-	0	-	-	-	-	10	-	-	-	-	16	9	-	-	-	-	-	-	12	-	-	4	-	17	-	-	-
10	-	-	5	0	18	16	-	-	-	3	6	-	-	-	0	10	7	-	5	-	-	4	4	-	10	-	5	-	7	-	19	-
11	-	6	-	-	-	-	-	7	2	-	-	-	-	9	-	-	-	-	-	20	-	-	-	4	-	19	-	-	-	-	-	10
12	18	-	-	-	-	-	0	-	-	-	-	10	16	-	-	-	-	9	-	-	-	12	-	-	-	-	-	4	-	17	-	-

Figure 2-4-2 Parity check matrices of rate-5/8

(672,504), Code rate: 3/4

	1	2	3	4	5	6	7	8	9	10	11	12	13	14	15	16	17	18	19	20	21	22	23	24	25	26	27	28	29	30	31	32
1	0	-	-	5	-	18	16	-	-	-	3	6	10	-	-	0	-	7	-	5	-	-	4	4	-	10	-	5	-	-	-	
2	-	18	6	-	7	-	-	0	10	2	-	-	-	16	9	-	20	-	9	-	4	12	-	-	4	-	19	-	-	-	-	
3	5	0	-	-	-	-	18	16	6	-	-	3	0	10	-	-	5	-	7	-	4	-	-	4	5	-	10	-	19	-	-	
4	-	-	18	6	0	7	-	-	-	10	2	-	-	-	16	9	-	20	-	9	-	4	12	-	-	4	-	19	-	10	-	
5	-	5	0	-	16	-	-	18	3	6	-	-	-	0	10	-	-	5	-	7	4	4	-	-	-	5	-	-	-	-	-	
6	6	-	-	18	-	0	7	-	-	-	10	2	9	-	-	16	9	-	20	-	-	-	4	12	19	-	-	-	-	-	-	
7	-	-	5	0	18	16	-	-	-	3	6	-	-	-	0	10	7	-	5	-	-	4	4	-	10	-	5	-	7	-	19	-
8	18	6	-	-	-	-	0	7	2	-	-	10	16	9	-	-	-	9	-	20	12	-	-	4	-	19	-	4	-	17	-	10

Figure 2-4-3 Parity check matrices of rate-3/4

(672,588), Code rate: 7/8

	1	2	3	4	5	6	7	8	9	10	11	12	13	14	15	16	17	18	19	20	21	22	23	24	25	26	27	28	29	30	31	32
1	0	18	6	5	7	18	16	0	10	2	3	6	10	16	9	0	20	7	9	5	4	12	4	4	4	10	19	5	10	-	-	-
2	5	0	18	6	0	7	18	16	6	10	2	3	0	10	16	9	5	20	7	9	4	4	12	4	5	4	10	19	19	10	-	-
3	6	5	0	18	16	0	7	18	3	6	10	2	9	0	10	16	9	5	20	7	4	4	4	12	19	5	4	10	17	19	10	-
4	18	6	5	0	18	16	0	7	2	3	6	10	16	9	0	10	7	9	5	20	12	4	4	4	10	19	5	4	7	17	19	10

Figure 2-4-4 Parity check matrices of rate-7/8

2.3.2.2 Bit Interleaver

The bits may be interleaved by a block interleaver which provides robustness against burst errors. The interleaving is performed upon encoded bits with an interleaving depth covering 4 LDPC codewords, over 2688 bits.

The block interleaving process is performed using a permutation rule $L(k)$. That is, the k^{th} output, written to location k in the output vector, is read from location $L(k)$

in the input vector. The block interleaving algorithm $L(k) = I^j_{p,q}(k)$ is described by four parameters: the block size $K_B = 2688$, an integer parameter p setting the partition size, an integer parameter q , and the iteration j governing the interleaving spreading. The relationship between the block of K_B coded bits, a_0, a_1, \dots, a_{K-1} , and the block of K_B interleaved bits, b_0, b_1, \dots, b_{K-1} , is given by:

$$b(k) = a[I^j_{p,q}(k)] \quad (2-9)$$

The interleaving rule for the 1st and the j^{th} iteration is defined as:

$$I^1_{p,q}(k) = \text{mod} \left[K_B - p + k + q \cdot p \cdot \text{mod}(-k - p \cdot k, K_B), K_B \right] \quad (2-10)$$

$$I^j_{p,q}(k) = \text{mod} \left[K_B - p + k + q \cdot p \cdot \text{mod}(-k - p \cdot I^{j-1}_{p,q}(k), K_B), K_B \right] \quad (2-11)$$

And the binary interleaving parameters shall be: $p = 24, q = 2, j = 1$. The following figure is an iterative structure of the interleaver.

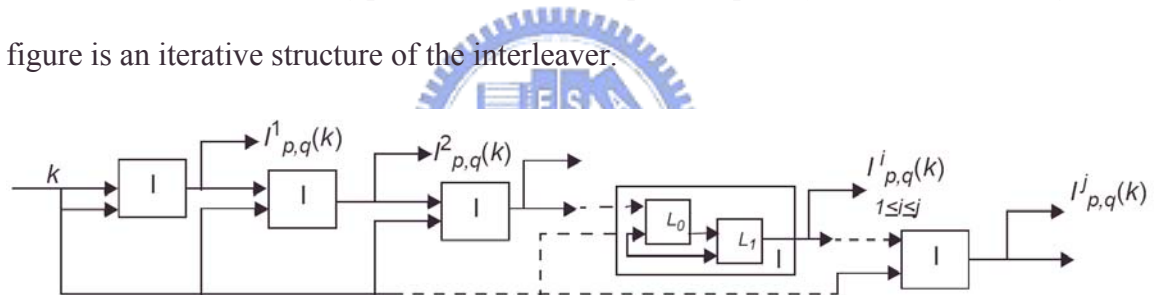


Figure 2-5 Bit interleaver structure

2.3.3 Constellation Mapping

The coded and interleaved binary serial input data, b_i , where $i = 0, 1, 2, \dots$, shall be modulated using QPSK, 16-QAM or 64-QAM modulation. The binary serial stream shall be divided into groups of 2, 4, or 6 bits and converted into complex numbers representing QPSK, 16-QAM or 64-QAM constellation points. The conversion shall be performed according to Gray-coded constellation mappings, illustrated in Figure 2-6 below.

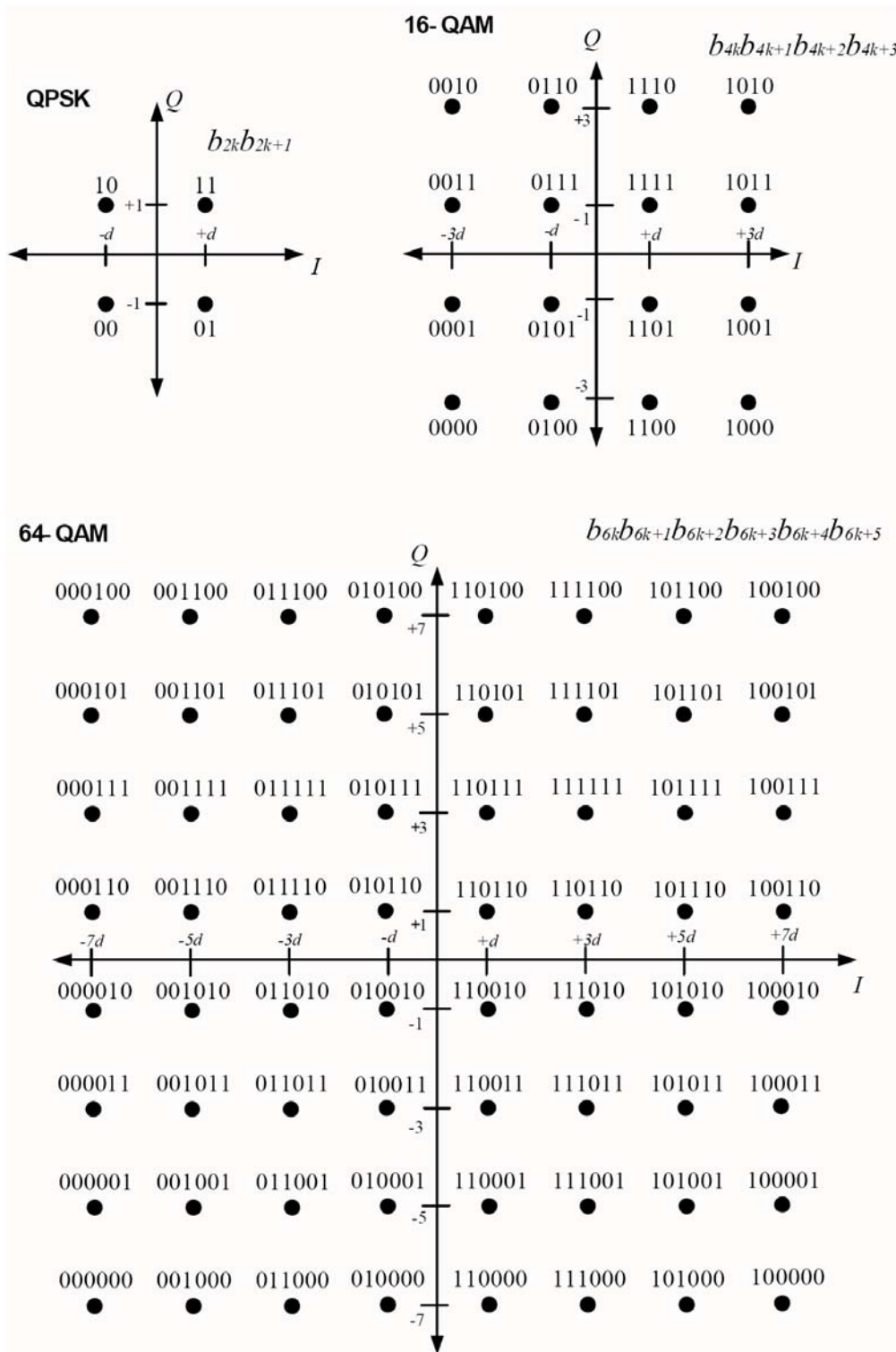


Figure 2-6 QPSK, 16-QAM, 64-QAM constellation bits encoding

The output values, a_k , where $k = 0, 1, 2, \dots$, are formed by multiplying the resulting value $(I_k + jQ_k)$ by a normalization factor K_{MOD} , as $a_k = (I_k + jQ_k) \times K_{MOD}$, and d in Table 2-5 is 1 when using normal constellation, 1.25 when using skewed

constellation.

Modulation	K_{MOD}
QPSK	$1/\sqrt{1+d^2}$
16-QAM	$1/\sqrt{5(1+d^2)}$
64-QAM	$1/\sqrt{21(1+d^2)}$

Table 2-5 Modulation dependent normalization factor

2.3.4 Spreader

For the spreading factor of 1, the modulated QPSK and QAM complex values a_k , where $k = 0, 1, 2, \dots$ at the output of the constellation mapper shall be grouped into sets of 336 complex numbers. Each group shall be assigned to an OFDM symbol.

This is denoted by the complex number $b_{k,n}$ as

$$b_{k,n} = a_{k+n \times 336}, \text{ for } k = 0, 1, \dots, 335, n = 0, 1, 2, \dots \quad (2-12)$$

where n is the OFDM symbol number.

For the spreading factor of 48, the modulated QPSK complex values $a(k)$, where $k = 0, 1, 2, \dots$ at the output of the constellation mapper shall be grouped into sets of seven complex numbers. This is denoted by the complex number $a_{k,n}$ as

$$a_{k,n} = a_{k+n \times 28}, \text{ for } k = 0:6, n = 0, 1, 2, \dots \quad (2-13)$$

where n is the group number. Each group shall be spread by a factor of 48 to generate a block of 336 complex numbers as follows:

$$\begin{aligned} b_{k,n} &= q_{\text{floor}(k/28)} a_{k,n}, \quad \text{for } k = 0:167 \\ b_{k,n} &= b_{335-k,n}^*, \quad \text{for } k = 168:335 \end{aligned} \quad (2-14)$$

where q is a sequence of length 24 given by:

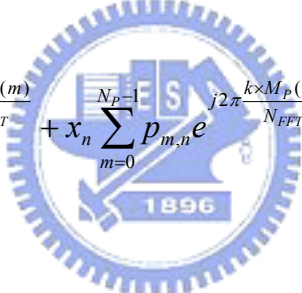
$$q = [+1 +j -1 +j +j +1 -1 +j -j +j -1 -j -1 +1 +1 +1 +j -j -1 -1 -1 +j -j +j] \quad (2-15)$$

2.3.5 Tone Interleaver

The tone-interleaver is a bit-reversal tone interleaver which may be combined with the IFFT operation to reduce implementation complexity. The tone interleaver shall be applied to data tones only. Tone interleaver operation is performed by first grouping the complex numbers $a_k = I_k + jQ_k$ at the output of the constellation mapping into blocks of 336 complex numbers.

2.3.6 HSI PHY OFDM modulator

The discrete-time signal for the n^{th} OFDM symbol is given by

$$s_{k,n} = \frac{1}{\sqrt{N_{FFT}}} \left[\sum_{m=0}^{N_D-1} d_{m,n} e^{j2\pi \frac{k \times M_D(m)}{N_{FFT}}} + x_n \sum_{m=0}^{N_P-1} p_{m,n} e^{j2\pi \frac{k \times M_P(m)}{N_{FFT}}} + \sum_{m=0}^{N_G-1} g_{m,n} e^{j2\pi \frac{k \times M_G(m)}{N_{FFT}}} \right] \quad (2-16)$$


where $k \in [0: N_{FFT} - 1]$, N_D is the number of data subcarriers, N_P is the number of pilot subcarriers, N_R is the number of reserved subcarriers, N_G is the number of guard subcarriers, N_{FFT} is the number of total subcarriers, and $d_{m,n}$, $p_{m,n}$, and $g_{m,n}$, are the complex numbers placed on the m^{th} data, pilot, and guard subcarriers of the n^{th} OFDM symbol, respectively.

The functions $M_D(m)$, $M_P(m)$, and $M_G(m)$ define a mapping between the indices $[0: N_D - 1]$, $[0: N_P - 1]$, $[0: N_R - 1]$, and $[0: N_G - 1]$ into the logical frequency offset index $[-N_{FFT}/2 : N_{FFT}/2 - 1]$. The definition for the mapping functions are given below:

$$M_D(m) = \begin{cases} m-177 + \text{round}(m/21) & 0 \leq m \leq 167 \\ m-174 + \text{round}[(m+1)/21] & 168 \leq m \leq 335 \end{cases}$$

$$M_P(m) = \begin{cases} -166 + m \times 22 & 0 \leq m \leq 7 \\ 12 + (m - 8 \times 22) & 8 \leq m \leq 15 \end{cases} \quad (2-17)$$

$$M_G(m) = \begin{cases} -185 + m & 0 \leq m \leq 7 \\ 170 + m & 8 \leq m \leq 15 \end{cases}$$

The mapping of data and pilot subcarriers within an OFDM symbol is illustrated in Figure 2-6. The mapping is further summarized in Table 2-6. As shown in Figure 2-6, there are 16 groups of subcarriers where each group is constituted of 21 data subcarriers and one pilot subcarrier.

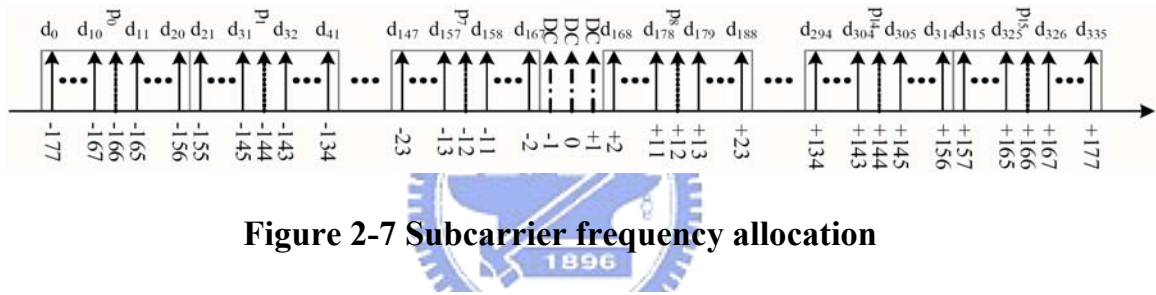


Figure 2-7 Subcarrier frequency allocation

Subcarriers type	Number of subcarriers	Logical subcarriers indexes
Null subcarriers	141	$[-256: -186] \cup [186:255]$
DC subcarriers	3	-1, 0, 1
Pilot subcarriers	16	$[-166:22: -12] \cup [12:22:166]$
Guard subcarriers	16	$[-185: -178] \cup [178:185]$
Data subcarriers	336	All others

Table 2-6 Subcarrier frequency allocation

2.3.7 Pilot subcarriers

In all OFDM symbols following the frame preamble, 16 of the subcarriers shall be dedicated to pilot signals for residual frequency offset tracking and phase noise

suppression. These pilot signals shall be placed into logical frequency subcarriers -166, -144, -122, -100, -78, -56, -34, -12, 12, 34, 56, 78, 100, 122, 144, and 166. The information for the m^{th} pilot subcarrier of the n th OFDM symbol shall be defined as follows:

$$p_m = \begin{cases} (1+j)/\sqrt{2} & \text{for } m = 0, 3, 5, 7, 9, 13, 15 \\ (1-j)/\sqrt{2} & \text{for } m = 1, 2, 4, 6, 8, 10, 11, 12, 14 \end{cases} \quad (2-18)$$

2.3.8 Guard subcarriers

In all OFDM symbols following the frame preamble, there shall be 16 guard subcarriers, 8 on each edge of the occupied frequency band, at the logical frequency subcarriers -185, -184, ..., -178 and 178, 179, ..., 185. The data on these subcarriers shall be left to the implementer. Individual implementations may exploit these guard subcarriers for various purposes, including relaxing the specifications on analog transmit and analog receive filters, and possibly peak to average power ratio reduction.

Chapter 3 IEEE 802.15.3c Receiver Design

3.1 Inner receiver structure

An OFDM receiver consists of an inner and outer receiver. The inner receiver conducts synchronization related operations while the outer receiver conducts FEC decoding. The block diagram of the inner receiver is shown in Figure 3-1.

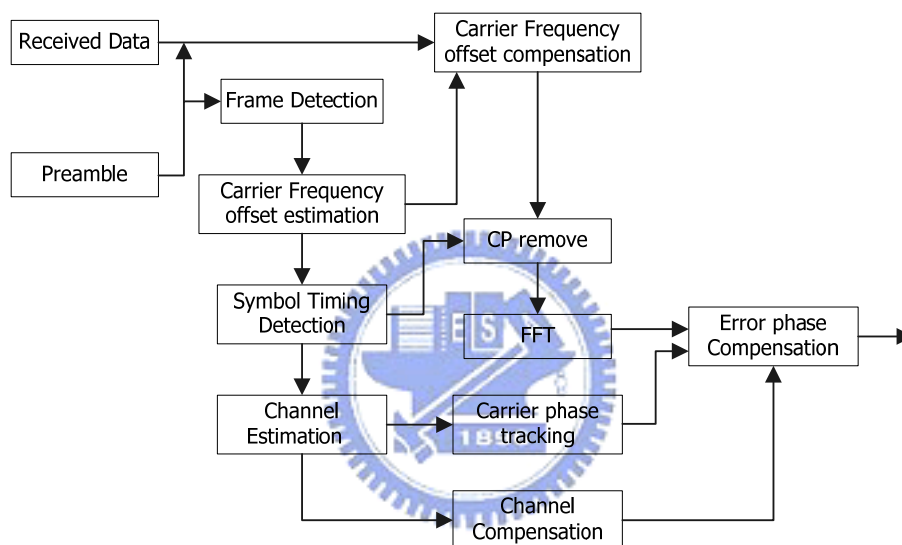


Figure 3-1 Signal flow structure of inner receiver

Detailed operations of the inner receiver conducts include frame detection, timing acquisition, frequency recovery, frame synchronization, and channel estimation. With proper synchronization of the inner receiver, the outer receiver can recover the transmitter data reliably.

3.2 Frame Detection

Frame detection is the task of finding an approximate estimate of the start of the preamble of an incoming data packet. The preamble structure defined in IEEE

802.15.3c HSI mode enables the receiver to use a simple and efficient algorithm to detect the packet. The algorithm we used is called the delay-and-correlate algorithm, which takes advantage of the periodicity of the SYNC (packet synchronization field) word at the start of the preamble. Figure 3-2 shows the signal flow structure of this algorithm.

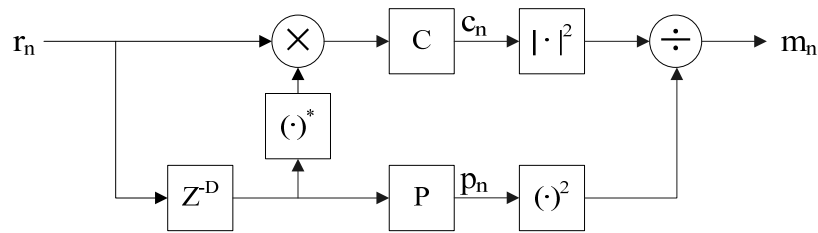


Figure 3-2 Signal flow structure of the delay and correlate algorithm

The figure shows two sliding windows C and P. The window C is used to calculate the crosscorrelation between the received signal and a delay version of the received signal. The delay D is equal to the period of the preamble. In the SYNC field, there contains 128 repetitions of a length 128 complementary Golay sequence \mathbf{c}_{128} . We choose $D=16 \times 128$. The window P is used to calculate the received signal energy. The value of the P window is then used to normalize the decision statistic, so that it is independent on the absolute received power level. The decision variable of this algorithm is calculated as

$$c_n = \sum_{k=0}^{L-1} r_{n+k} r_{n+k-D}^* \quad (3-1)$$

$$p_n = \sum_{k=0}^{L-1} r_{n+k+D} r_{n+k+D}^* \quad (3-2)$$

$$m_n = \frac{|c_n|^2}{(p_n)^2} \quad (3-3)$$

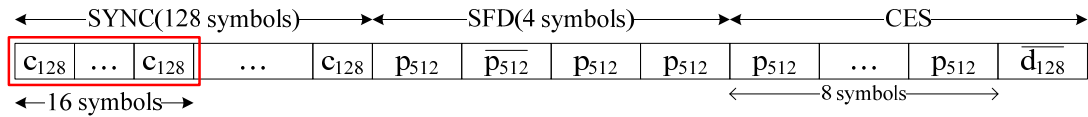


Figure 3-3 Preamble used for frame detect

The decision variable m_n is confined between 0 and 1. When the received signal only consists of noise, the output c_n of the delayed crosscorrelation is a zero-mean random variable. Once the start of the packet is received, c_n is a crosscorrelation of two sets of sixteen c_{128} symbols. Therefore, m_n will jump up quickly to its maximum value, and it can serve as a good indicator of the start of the packet.

3.3 Frequency Synchronization

Both the transmitter and the receiver use their own oscillators to generate carriers and sampling signals. Because of it, the signal generated from the receiver never has the same frequency as it generated from the transmitter. The frequency difference between the transmitter and receiver oscillator is called frequency offset.

One of the main drawbacks of OFDM is its sensitivity to the carrier frequency offset. The carrier frequency offset will reduce the amplitude of subcarriers and cause intercarrier interference (ICI). The preamble allows the receiver to use an efficient maximum likelihood algorithm to estimate and correct for the frequency offset. Let the transmitter signal be s_n , and the complex baseband model of the passband signal y_n be

$$y_n = s_n e^{j2\pi f_{tx} n T_s} \quad (3-4)$$

where f_{tx} is the transmitter carrier frequency, and T_s is the sampling period. After the receiver downconverts the signal with a carrier frequency f_{rx} , the received

complex baseband signal r_n without the noise term is

$$\begin{aligned}
 r_n &= s_n e^{j2\pi f_{tx} n T_s} e^{-j2\pi f_{rx} n T_s} \\
 &= s_n e^{j2\pi (f_{tx} - f_{rx}) n T_s} \\
 &= s_n e^{j2\pi f_{\Delta} n T_s}
 \end{aligned} \tag{3-5}$$

where $f_{\Delta} = f_{tx} - f_{rx}$ is the difference between the transmitter and receiver carrier frequencies. Let D be the delay between the identical samples of the 12 repeated c_{128} symbols at the end of SYNC sequence.

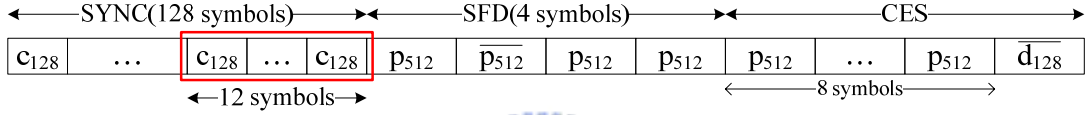


Figure 3-4 Preamble used for frequency synchronization

Define an autocorrelation term as

$$\begin{aligned}
 z &= \sum_{n=0}^{L-1} r_n r_{n+D}^* \\
 &= \sum_{n=0}^{L-1} s_n e^{j2\pi f_{\Delta} n T_s} (s_{n+D} e^{j2\pi f_{\Delta} (n+D) T_s})^* \\
 &= \sum_{n=0}^{L-1} s_n s_{n+D}^* e^{j2\pi f_{\Delta} n T_s} e^{-j2\pi f_{\Delta} (n+D) T_s} \\
 &= e^{j2\pi f_{\Delta} D T_s} \sum_{n=0}^{L-1} |s_n|^2
 \end{aligned} \tag{3-6}$$

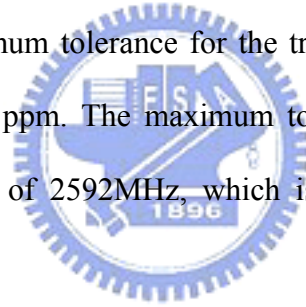
Equation (3-6) is a sum of complex variables with an angle proportional to the frequency offset. Thus, the frequency offset can then be estimated as:

$$\hat{f}_{\Delta} = -\frac{1}{2\pi D T_s} \angle z \tag{3-7}$$

There is a limitation of the method shown above, i.e., its operating range. The operating range defines how large the frequency offset can be estimated. The range is directly related to the period of the repeated symbols. The angle of z is of the form $-2\pi f_{\Delta}DT_s$, which is unambiguously defined only in the range $[-\pi, \pi)$. Thus, if the absolute value of the frequency error is larger than the following limit,

$$|f_{\Delta}| \geq \frac{\pi}{2\pi DT_s} = \frac{1}{2DT_s} \quad (3-8)$$

the estimate will be incorrect. This is because z has rotated an angle large than π . For the SYNC sequence, the sample time T_s is 0.39ns, and the delay D is 1536 (12×128). Thus, the maximum frequency error that can be estimated is 834.67 kHz. This should be compared with the maximum allowable frequency error defined in the 802.15.3c system. The maximum tolerance for the transmitted center frequency and chip clock frequency is ± 20 ppm. The maximum tolerable frequency error is then 103.68kHz for the chip rate of 2592MHz, which is well within the range of the estimation.



3.4 Symbol Timing

The performance of the symbol timing algorithm directly influences the tolerance of the maximum delay spread of the channel. Specifically, the algorithm is used to locate the starting position of a DFT window. An OFDM receiver achieves its maximum delay spread tolerance when the DFT window starts at the first sample of an OFDM symbol.

As mentioned above, the start edge of a packet can be estimated by the frame detector. This estimate can then be seen as a coarse symbol timing. Since the receiver knows the preamble, it can further use a crosscorrelation based algorithm to refine the

timing. Let t_k be a known reference sequence (a portion of the preamble). Then, we can estimate the starting time of the symbol as.

$$\hat{t}_s = \arg \max_n \left| \sum_{k=0}^{L-1} r_{n+k} t_k^* \right|^2 \quad (3-9)$$

where L is the length of the reference sequence. The value of L determines the performance of the algorithm. A larger value will improve the performance, but also increase the computational complexity. We select two SFD sequences as the reference signal here, which includes two p_{512} sequences.

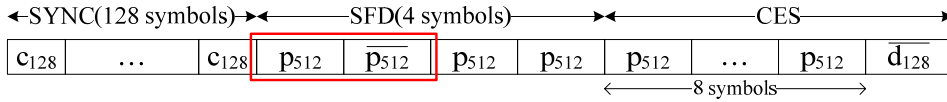
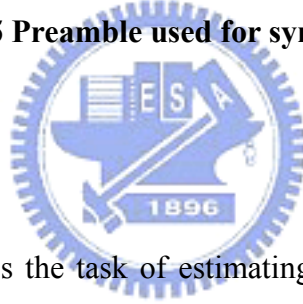


Figure 3-5 Preamble used for symbol timing

3.5 Channel Estimation



The channel estimation is the task of estimating the frequency response of the channel that transmitted signal travels before reaching the receiver antenna. We generally assume that the channel is quasi-stationary, which means the channel response does not change during a data packet. Therefore, we only need to estimate the channel once during one packet transmission. We use the CES symbols to estimate the channel response.

The first eight p_{512} sequences in CES are identical. We can take the advantage of this property to improve the quality of channel estimation. After the DFT, the received CES symbol $R_{l,k}$ is known to be a product of the CES symbol X_k and the channel H_k plus additive noise $N_{l,k}$, i.e.,

$$R_{l,k} = H_k X_k + N_{l,k} \quad l = 1 \dots n, \quad n \leq 8 \quad (3-10)$$

where n is the number of symbols used for channel estimation.

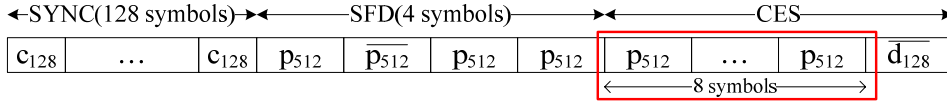


Figure 3-6 Preamble used for channel estimation

Thus the channel response can then be calculated as

$$\begin{aligned}
 \hat{H}_k &= \frac{1}{n}(R_{1,k} + R_{2,k} + \dots + R_{n,k}) / X_k \\
 &= \frac{1}{n}(H_k X_k + N_{1,k} + H_k X_k + N_{2,k} \dots + H_k X_k + N_{n,k}) / X_k \\
 &= \frac{1}{n}(H_k + \dots + H_k + \frac{N_{1,k}}{X_k} + \dots + \frac{N_{n,k}}{X_k}) \\
 &= H_k + \frac{1}{n}(N_{1,k} + \dots + N_{n,k}) / X_k \tag{3-11}
 \end{aligned}$$

The noise samples are statistically independent, thus the variance of their n -term average will be reduced to $1/n$ of the original variance. If n is larger, we can have better estimate with the price of higher computational complexity.

The channel estimation can also be conducted in the time domain. We can calculate the crosscorrelation of the received signal r_n and a known reference p_k , which is a CES symbol with length L . Theoretically, the resultant signal will give an estimate of the time-domain channel response. To locate the whole response more precisely, we can first find the position of the maximum channel tap which corresponds to the position giving the peak crosscorrelation value, i.e.,

$$peak = \arg \max_n \left| \sum_{k=0}^{L-1} r_{n+k} p_k^* \right|^2 \tag{3-12}$$

After finding the peak position, we can search backward and forward for 64 taps to locate an area having the maximum energy. We set the number of 64 because the

maximum CP length is 64. Find the average of these 64 taps, set the value to zero which is smaller than average. Then the residual taps are estimated impulse response of channel.

3.6 Phase Tracking

There will always be an error associated with the carrier frequency estimation. Thus, there still have some residual frequency error after the frequency offset compensation. The main problem caused by the residual frequency offset is the constellation rotation (phase error), which will influence the demodulation. In this section, we will discuss the phase tracking problem. We first use a data-aided tracking method which exploits the pilot subcarriers to track the phase error. In 802.15.3c, there are 16 pilot subcarriers in the high speed interface mode. With the residual frequency error, the received pilot subcarriers $R_{n,k}$ will be equal to the product of the channel frequency response H_k , the known pilot subcarrier $P_{n,k}$, and an phase error, i.e.,

$$R_{n,k} = H_k P_{n,k} e^{j2\pi n f_\Delta} \quad (3-13)$$

With the estimated channel response \hat{H}_k , we can estimate the phase error as

$$\begin{aligned} \hat{\Phi}_n &= \angle \left[\sum_{k=1}^{N_p} R_{n,k} (\hat{H}_k P_{n,k})^* \right] \\ &= \angle \left[\sum_{k=1}^{N_p} H_k P_{n,k} e^{j2\pi n f_\Delta} (\hat{H}_k P_{n,k})^* \right] \quad \text{if } \hat{H}_k \text{ is perfect estimated} \\ &= \angle \left[\sum_{k=1}^{N_p} |H_k|^2 |P_{n,k}|^2 e^{j2\pi n f_\Delta} \right] \quad P_{n,k} = (1 \pm i) / \sqrt{2} \end{aligned}$$

$$= \angle \left[e^{j2\pi n f_{\Delta}} \sum_{k=1}^{N_p} |H_k|^2 \right] \quad (3-14)$$

To have a more accurate estimation result, we will use a feedback type phase tracking algorithm [2]. The block diagram of the algorithm is shown below.

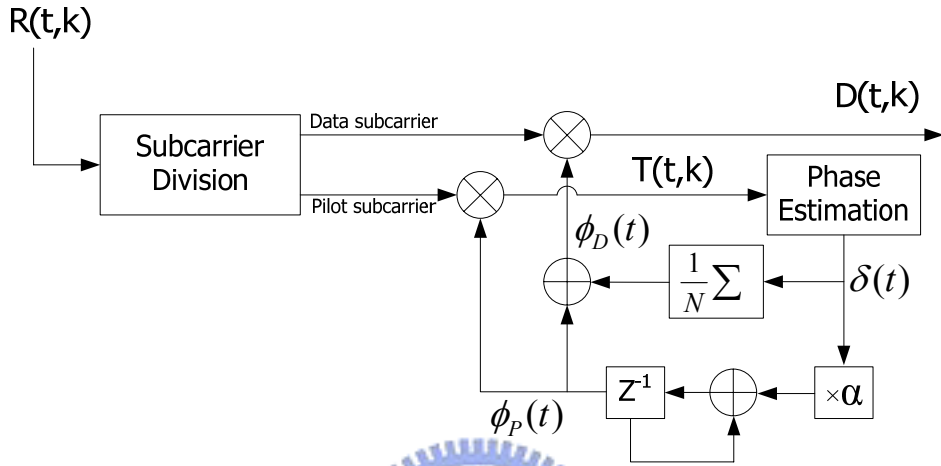


Figure 3-7 Signal flow structure of phase compensator

The output of the function block “phase estimation” denote as $\delta(t)$ that can be obtain by the following procedure

$$T(t,k) = R(t,k) \cdot \exp(-j\phi_p(t)) \quad (3-15)$$

$$\delta(t) = \frac{1}{16} \sum_{k \in K_p} \arg(S(k), T(t,k)) \quad (3-16)$$

where K_p denote the index of 16 pilot subcarriers, $T(t,k)$ is a coarse compensated value, and $S(k)$ is the pilot subcarrier data. The final output $\delta(t)$ calculate the phase error form $T(t,k)$ and $S(k)$. The pilot subcarrier phase compensation value $\phi_p(t)$ is represented as

$$\phi_p(0) = 0, \quad \phi_p(t) = \phi_p(t-1) + \alpha\delta(t), \quad 0 < \alpha < 1 \quad (3-17)$$

The summation and average block is used for data subcarrier phase compensation

after the phase estimation block. The phase compensation values for data subcarriers and phase compensation with this value are represented as follows

$$\phi_D(0) = 0, \quad \phi_D(t) = \phi_P(t) + \frac{1}{N} \sum_{i=t-N+1}^t \delta(i) \quad (3-18)$$

$$D(t, k) = R(t, k) \cdot \exp(-j\phi_D(t-1)) \quad , k \in K_D \quad (3-19)$$

where K_D is the set of index of data subcarriers.



Chapter 4 Spatial Division Multiple Access in IEEE802.15.3c Systems

4.1 Introduction

As we know, the IEEE 802.15.3c millimeter-wave alternative physical layer for personal area networks (PAN) can reach high data rate over 1GHz. But it endures some problems such as severe path loss from oxygen absorption and high penetration loss in 60GHz band. To overcome these problems, high gain and high directivity antennas are usually required to compensate for the loss. An effective solution achieving the goals is the use of planar antenna arrays, which can be used to conduct beamforming. An example of an 8×8 planar array is shown in Figure 4-1. Note that in the example patch antennas are used. Since the wavelength of the 60GHz signal is short, the antenna array can be fabricated in a small-size silicon. Each of the patch antenna is equipped with a phase shift circuit. By adjusting the phase shift of each antenna, we can steer the beam direction. Note that the phase adjustment is done in the analogy domain. There are two problems with the analog beamforming. The first is that the number of the phases we can adjust may be limited and the phase we adjust may not be accurate. The second is that it can only adjust phase not the amplitude and it cannot conduct interference cancellation.

A more flexible approach is to use the digital beamforming. However, this will require a large amount of digital-to-analogy (D/A) and analog-to-digital (A/D) devices and the implementation cost is greatly enhanced. Recently, a hybrid approach has been proposed [3]-[5], whose block diagram is shown in Figure 4-2. With a limited number of D/A and A/D devices, this approach uses the analogy and digital beamforming simultaneously. In this chapter, we will use the hybrid antenna array to implement the spatial division multiple access (SDMA) in IEEE 802.15.3c system.

Note that a local area network has been defined in IEEE 802.15.3c. The use of the SDMA technique can greatly enhance the efficiency of the network.

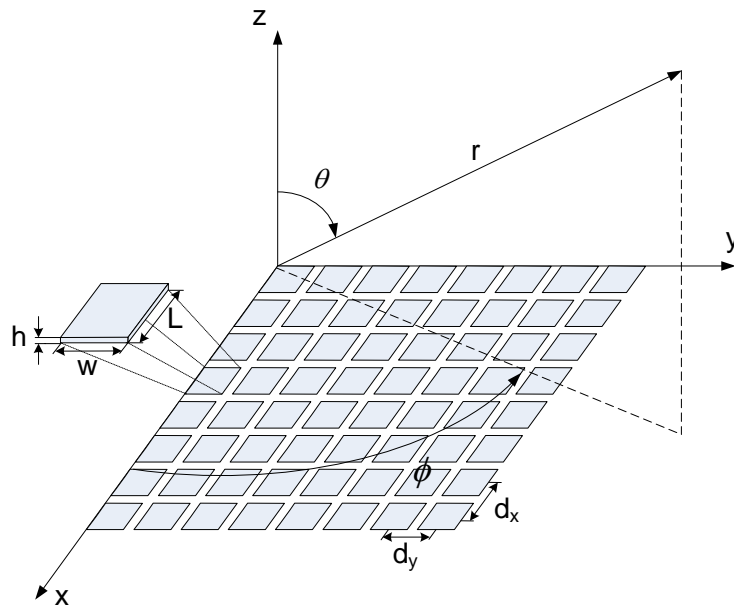


Figure 4-1 Architecture of planar antenna arrays

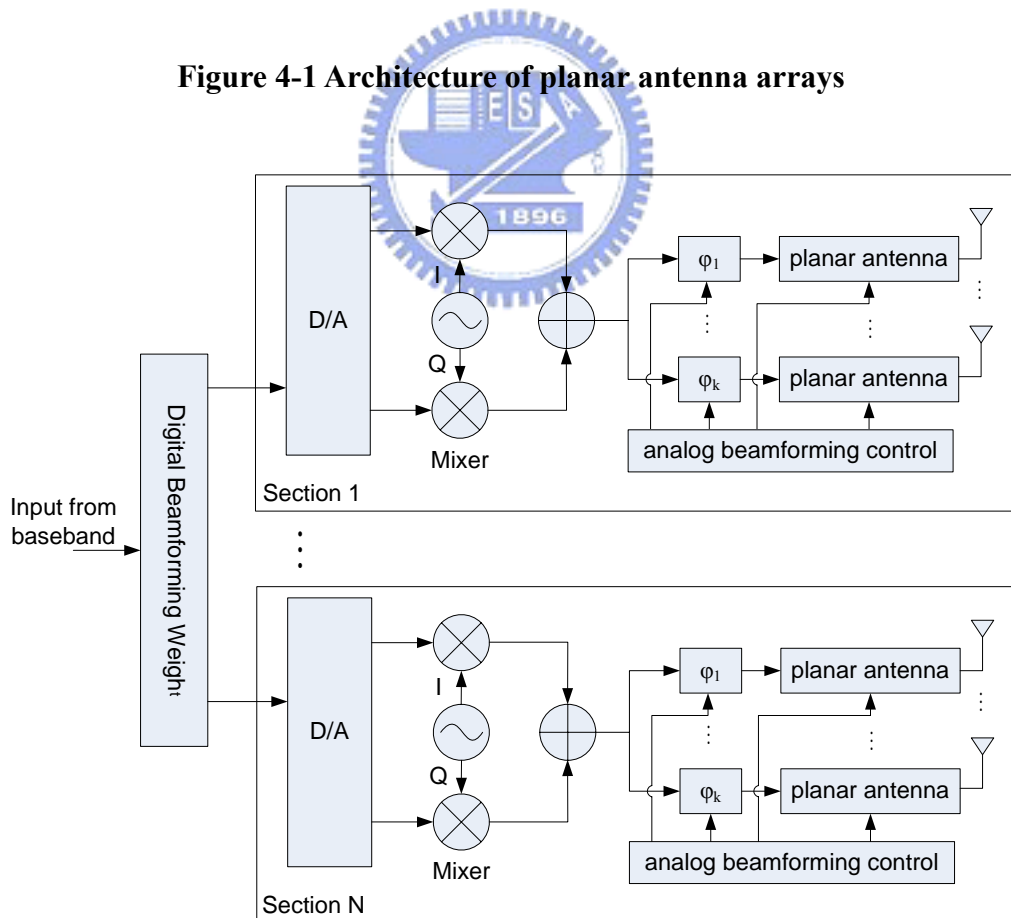


Figure 4-2 Block diagram of Hybrid Beamforming

4.2 Architecture of planar antenna arrays

The planar antenna array defined in [6] has 64 identical patch antennas which form an 8×8 antenna matrix. As mentioned, each antenna element has its own phase shifter to manipulate the phase of signal go through it. By beamforming the array to multiple directions, we can conduct the SDMA scheme. There are four D/A and A/D devices in the system. We assume that there are at most two users who a transmitter/receiver can communicate with. The planar antenna array can be partitioned into two kinds of configuration, 1×1 and 1×2 sections. For configuration 1, all patch antennas are used to support a single user. For configuration 2, the whole 8×8 planar antenna array is partitioned into two sections. Each section can serve a user with an 8×4 antenna arrays. In configuration 2, the signal of a user will be interfered by the signal from the other user. As a result, we have to conduct interference cancellation.

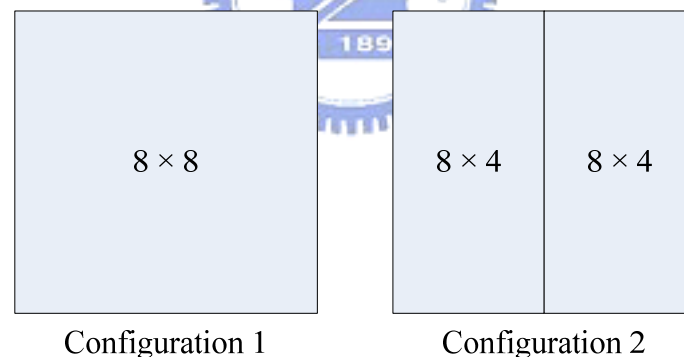


Figure 4-3 Configuration of planar antenna arrays

4.3 The array pattern of planar antenna arrays [6]

The entire array pattern for a configuration section is computed as the product of the single antenna pattern of the electric field, the analog beamforming pattern and digital beamforming pattern.

The far-zone electric field of a single antenna element is given as

$$E(\phi, \theta) = E_\theta \vec{a}_\theta + E_\phi \vec{a}_\phi + E_r \vec{a}_r \quad \text{where } E_r \cong 0 \quad (4-1)$$

$$E_\theta = j \frac{hWkE_0 e^{-jkr}}{\pi r} \left[\cos \phi \cos X \left(\frac{\sin Y}{Y} \right) \left(\frac{\sin Z}{Z} \right) \right] \quad (4-2)$$

$$E_\phi = j \frac{hWkE_0 e^{-jkr}}{\pi r} \left[\cos \theta \sin \phi \cos X \left(\frac{\sin Y}{Y} \right) \left(\frac{\sin Z}{Z} \right) \right] \quad (4-3)$$

And the corresponding parameters are defined as

$$X \triangleq \frac{kL}{2} \sin \theta \cos \phi \quad (4-4)$$

$$Y \triangleq \frac{kW}{2} \sin \theta \sin \phi \quad (4-5)$$

$$Z \triangleq \frac{kW}{2} \cos \theta \quad k = \frac{2\pi}{\lambda} \quad (4-6)$$

where E_0 is a constant, W and L are width and length per single antenna element, d_x and d_y are the distance in the x and y directions of the adjacent patch antenna, and we set $d_x = d_y$ (as shown in Figure 4-1). The parameter $k = 2\pi/d_x = 2\pi/d_y$.

For a general $M \times N$ array, the array pattern of the digital beamforming is defined as [7]

$$DB(\phi, \theta) = \sum_{m=1}^M \sum_{n=1}^N w_{m,n} e^{j(m-1)\psi_x} e^{j(n-1)\psi_y} \quad (4-7)$$

$$\psi_x \triangleq kd_x \sin \theta \cos \phi \quad (4-8)$$

$$\psi_y \triangleq kd_y \sin \theta \sin \phi \quad (4-9)$$

In this algorithm, we want to steer the main lobe in the direction (ϕ_L, θ_L) and cancel the interference from the direction (ϕ_l, θ_l) where $l = 1, \dots, L-1$. Then the algorithm can be rewritten to satisfy the requirement.

$$DB(\phi, \theta) = \sum_{m=1}^M \sum_{n=1}^N w_{m,n} e^{j(m-1)\psi_x} e^{j(n-1)\psi_y}$$

$$= \sum_{l=1}^L b_l \left(\sum_{m=1}^M e^{j(m-1)(\psi_x - \psi_{xl})} \right) \left(\sum_{n=1}^N e^{j(n-1)(\psi_y - \psi_{yl})} \right) \quad (4-10)$$

And b_l can be solved by the following equation

$$A \begin{pmatrix} b_1 \\ \vdots \\ b_{L-1} \\ b_L \end{pmatrix} = \begin{pmatrix} 0 \\ \vdots \\ 0 \\ 1 \end{pmatrix} \quad (4-11)$$

$$A = \{a_{k,l}\}_{1 \leq k, l \leq L}, a_{k,l} = \sum_{m=1}^M e^{j(m-1)(\psi_{xk} - \psi_{xl})} \sum_{n=1}^N e^{j(n-1)(\psi_{yk} - \psi_{yl})} \quad (4-12)$$

The weight $w_{m,n}$ of digital beamforming pattern can be calculated by

$$w_{m,n} = \sum_{l=1}^L b_l e^{-j(m-1)\psi_{xl}} e^{-j(n-1)\psi_{yl}} \quad (4-13)$$

This algorithm is mainly to null the interference introduced by other users.

For analog beamforming, the effective weight for an antenna will be

$$w_{m,n} = e^{j(m-1)\beta_x} e^{j(n-1)\beta_y} \quad (4-14)$$

where β_x and β_y denotes the phase shifts along the x-axis and y-axis, respectively.

If the main beam in the section has been steered to θ_d and ϕ_d , it can be express as the following equations

$$\beta_x = -kd_x \sin \theta_d \cos \phi_d \quad (4-15)$$

$$\beta_y = -kd_y \sin \theta_d \sin \phi_d \quad (4-16)$$

Using (4-15) and (4-16) in (4-14), we can obtain the antenna pattern for the analogy beamforming. In analogy beamforming, it cannot null the interference from other users, and its performance will be inferior to digital beamforming if interference actually exists.

Now we consider hybrid beamforming with the planar antenna arrays of configuration 1 first. In this case, the overall array pattern is obtained with the

multiplication of the analog and digital beamforming patterns. We first partition the planar antenna arrays into four analog parts, part A, part B, part C and part D.

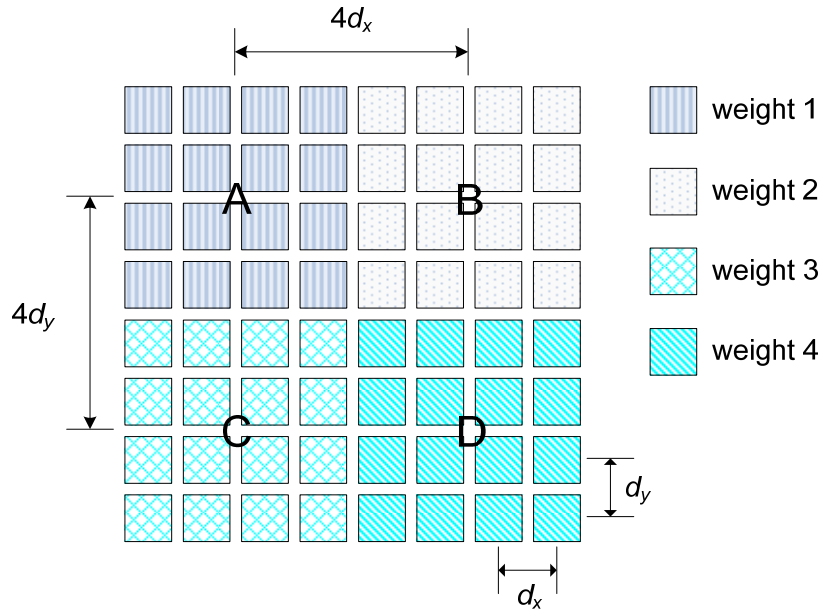


Figure 4-4 Initial structure of planar antenna arrays

Each of them has its own weight to form the digital beamforming pattern. According to this configuration, we can the antenna pattern as

$$DB(\phi, \theta) = w_1 + w_2 e^{jk4d_x \sin \theta \cos \phi} + w_3 e^{jk4d_y \sin \theta \sin \phi} + w_4 e^{jk4d_x \sin \theta \cos \phi} e^{jk4d_y \sin \theta \sin \phi} \quad (4-17)$$

where w_n for $n = 1, 2, 3, 4$ is corresponding to digital weight, and $4d_x$ and $4d_y$ denote the distance in the x and y directions of the adjacent analog parts. And the analog beamforming pattern of each part can be written multiplying two linear array factors along x-axis and y-axis, and present as

$$RF(\phi, \theta) = \sum_{m=0}^3 \sum_{n=0}^3 e^{jm(\psi_x + \beta_x)} e^{jn(\psi_y + \beta_y)} \quad (4-18)$$

ψ_x and ψ_y are the same parameter as (4-8) and (4-9).

But in this partition method, the antenna pattern has many four times of more sidelobes. Therefore, it cannot have the best performance. To solve this problem, we can rearrange the planar antenna arrays in some special way. In the previous method, we directly separate planar antenna arrays into four parts and every part has 16 antenna elements. Now we take one antenna element of each analog part to form a small group repeatedly, and then will have 16 small groups. Use these 16 groups to reconstruct the 8×8 planar antenna arrays as figure 4-4 shows. The analog and digital beamforming pattern can be rewritten as

$$RF(\phi, \theta) = \sum_{m=0}^3 \sum_{n=0}^3 e^{j2m(\psi_x + \beta_x)} e^{j2n(\psi_y + \beta_y)} \quad (4-19)$$

$$DB(\phi, \theta) = w_1 + w_2 e^{jkd_x \sin \theta \cos \phi} + w_3 e^{jkd_y \sin \theta \sin \phi} + w_4 e^{jkd_x \sin \theta \cos \phi} e^{jkd_y \sin \theta \sin \phi} \quad (4-20)$$

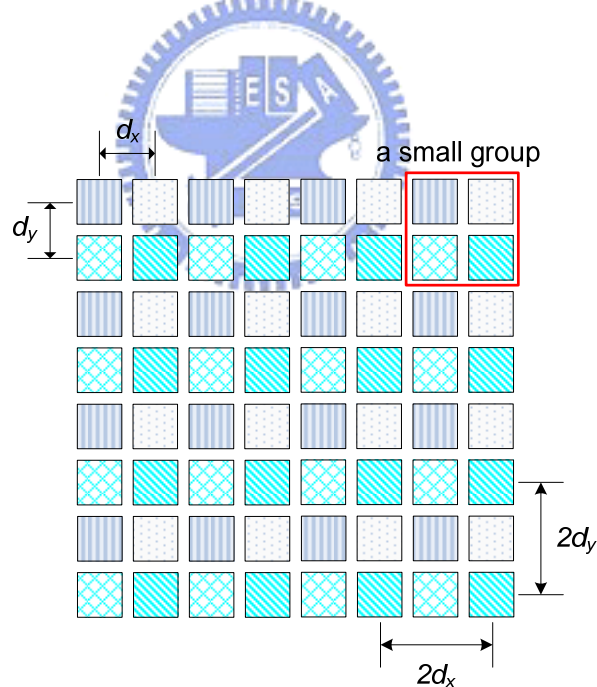


Figure 4-5 Rearrange structure of planar antenna arrays

In the view of digital beamforming pattern, distance between different different parts reduces to d_x and d_y . For analog beamforming pattern, distance between adjacent antenna element in each analog part along x-axis and y-axis extend to $2d_x$ and $2d_y$.

Next we consider about the planar antenna array of configuration 2. In configuration 2, we use two weights or four weights to form the digital beamforming for each user. The antenna array will be reconstructed as follow

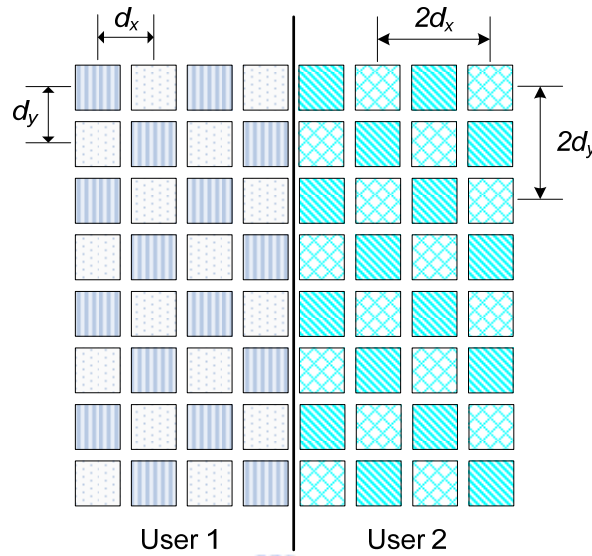


Figure 4-6 Planar antenna arrays of configuration 2 with two weights per user

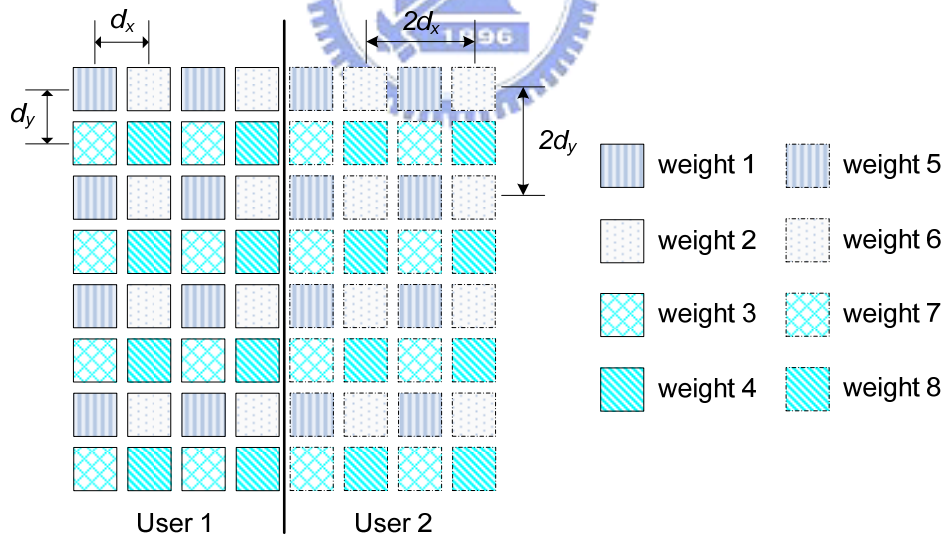


Figure 4-7 Planar antenna arrays of configuration 2 with four weights per user

The analog and digital beamforming pattern for user 1 for the case where two weights are used for each user can be represent as

$$RF(\phi, \theta) = \sum_{m=0}^1 \sum_{n=0}^3 e^{j2m(\psi_x + \beta_x)} e^{j2n(\psi_y + \beta_y)} \quad (4-21)$$

$$DB(\phi, \theta) = w_1(1 + e^{jkd_x \sin \theta \cos \phi} e^{jkd_y \sin \theta \sin \phi}) + w_2(e^{jkd_x \sin \theta \cos \phi} + e^{jkd_y \sin \theta \sin \phi}) \quad (4-22)$$

and for the case where four weights are used for each user can be represented as

$$RF(\phi, \theta) = \sum_{m=0}^1 \sum_{n=0}^3 e^{j2m(\psi_x + \beta_x)} e^{j2n(\psi_y + \beta_y)} \quad (4-23)$$

$$DB(\phi, \theta) = w_1 + w_2 e^{jkd_x \sin \theta \cos \phi} + w_3 e^{jkd_y \sin \theta \sin \phi} + w_4 e^{jkd_x \sin \theta \cos \phi} e^{jkd_y \sin \theta \sin \phi} \quad (4-24)$$

The quality of the received signal of a user can be seriously affected by the multiple access interference in the SDMA system in the analogy beamforming system. By using the hybrid beamforming, the main beam of user 1 can be adjusted towards the direction of the null array factors of user 2, and vice versa. In this way, we can achieve higher SINR at the desired direction.

4.4 MIMO modeling of SDMA systems

We want to model the SDMA system with the planar antenna arrays as a MIMO system. For a two-user beamforming system, we have from two beams pointing to two desired directions. When considering one user, the signal for the other user will be viewed as interference. Two examples of the beamforming pattern with two users are shown below.

I. Configuration 1

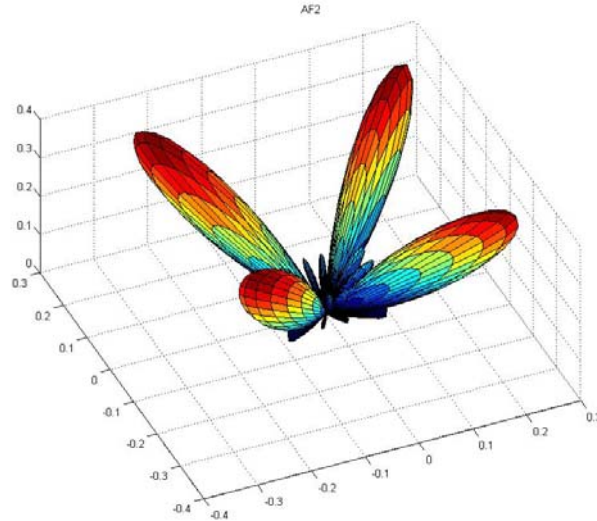


Figure 4-8 Beamforming pattern with two users (2 weights) between $\pi/2$

In this figure, we set θ as $\pi/4$ and ϕ for user 1 is $\pi/4$ for user 2 is $-\pi/4$. Note that two weights are used per user.

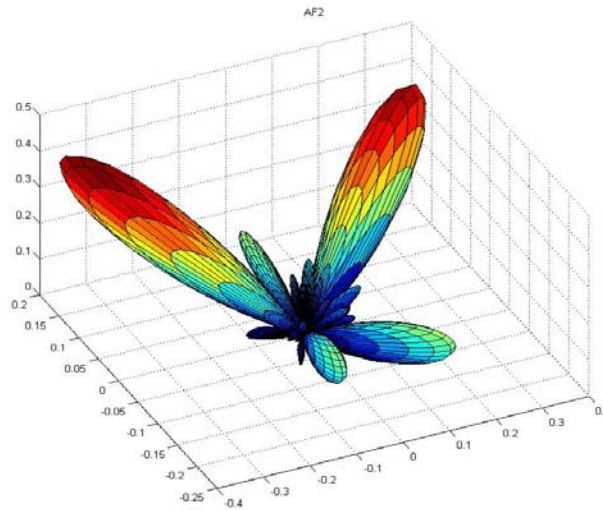


Figure 4-9 Beamforming pattern with two users (2 weights) between $3\pi/4$

In this figure, we set θ as $\pi/4$ and ϕ for user 1 is $\pi/8$ for user 2 is $7\pi/8$. Note that two weights are used per user.

II. Configuration 2

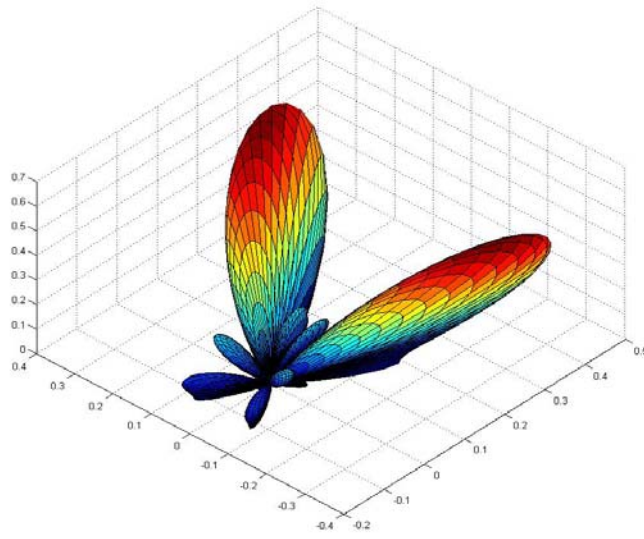


Figure 4-10 Beamforming pattern with two users (4 weights) between $\pi/2$

In this figure, we set θ as $\pi/4$ and ϕ for user 1 is $\pi/4$ for user 2 is $-\pi/4$. Note that four weights are used per user.

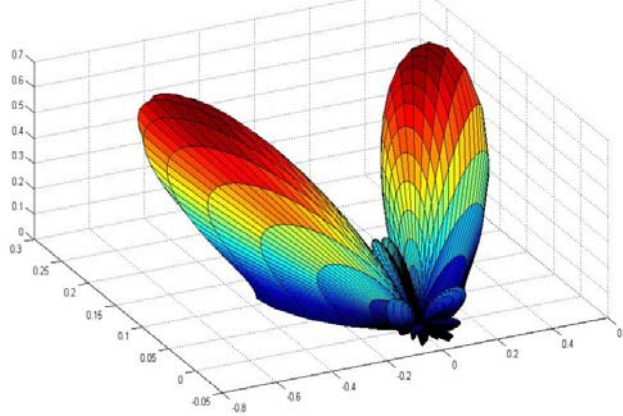


Figure 4-11 Beamforming pattern with two users (4 weights) between $3\pi/4$

In this figure, we set θ as $\pi/4$ and ϕ for user 1 is $\pi/8$ for user 2 is $7\pi/8$. Note that four weights are used per user.

If the desire user is user 1, the SINR of user 1 can be obtained by

$$SINR_{user1}(\phi, \theta) = \frac{|E(\phi, \theta)RF(\phi, \theta)_{user1}DB(\phi, \theta)_{user1}|^2}{|E(\phi, \theta)RF(\phi, \theta)_{user2}DB(\phi, \theta)_{user2}|^2 + \sigma_n^2} \quad (4-25)$$

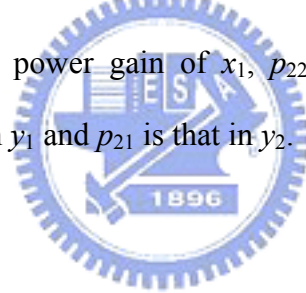
where σ_n^2 is the noise power, $E(\phi, \theta)$ is the electric field of the element antenna pattern given in (4-1). Using (4-25), we can calculate the power gain of the main beam and that of the interference beam. An MIMO model can then be established as

$$\begin{bmatrix} y_1 \\ y_2 \end{bmatrix} = \begin{bmatrix} p_1 & p_2 \\ p_2 & p_1 \end{bmatrix} \begin{bmatrix} x_1 \\ x_2 \end{bmatrix} + \begin{bmatrix} w_1 \\ w_2 \end{bmatrix} \quad (4-26)$$

where y_1, y_2 is the receive signal and x_1, x_2 is transmit data, p_1 is the main beam power gain, and p_2 is the interference power gain. Note here that we assume the receive/transmit power for two users is the same. For a general SDMA system, we may have

$$\begin{bmatrix} y_1 \\ y_2 \end{bmatrix} = \begin{bmatrix} p_{11} & p_{12} \\ p_{21} & p_{22} \end{bmatrix} \begin{bmatrix} x_1 \\ x_2 \end{bmatrix} + \begin{bmatrix} w_1 \\ w_2 \end{bmatrix} \quad (4-27)$$

where p_{11} is the main beam power gain of x_1 , p_{22} is that of user x_2 , p_{12} is the interference power received in y_1 and p_{21} is that in y_2 .



Chapter 5 MIMO Detectors in OFDM Systems

Spectrum is a limited resource in all wireless systems, for a single antenna system, the bandwidth fundamentally limits the possible data throughput. The Multi-Input Multi-Output (MIMO) technology can offer a significant gain in the spectral efficiency. And it can be used to either increase the transmission rate without increasing transmission power or bandwidth, or increase the diversity. Since the antenna array has been introduced to the wireless HDMI system, the application of the MIMO technology becomes feasible. In this chapter, we review some of popular MIMO detectors.

5.1 System Model

We first consider a Rayleigh flat-fading multipath MIMO channel model, with M transmit antennas and N receive antennas. The complex baseband transmit signal vector can be defined as $x(k) = [x_1(k), x_2(k), \dots, x_M(k)]^T$ and the received signal vector is $y(k) = [y_1(k), y_2(k), \dots, y_N(k)]^T$. The receive signal can then be expressed by

$$y(k) = Hx(k) + w(k) \quad (5-1)$$

$$H = \begin{bmatrix} h_{11} & h_{12} & \cdots & h_{1N} \\ h_{21} & h_{22} & \cdots & h_{2N} \\ \vdots & \vdots & \ddots & \vdots \\ h_{M1} & h_{M2} & \cdots & h_{MN} \end{bmatrix} \quad (5-2)$$

where H is a $M \times N$ complex channel matrix and its element h_{mn} is independent and identically distribution (i.i.d.) complex Gaussian random variables with zero mean and variance σ_n^2 , and $w(k) = [w_1(k), w_2(k), \dots, w_N(k)]^T$ is an independent and

identically distribution (i.i.d.) complex Gaussian noise vector. We assume that the fading coefficients will not change during the course of each MIMO transmission session.

According to IEEE 802.15.3c transmitter structure, a bit stream after passing through the spreader is mapped to OFDM symbols. In the MIMO system, we will de-multiplex this single input stream to N paths and each of the streams is mapped to OFDM symbols and transmitted with an individual antenna. Figure 4-1 and 4-2 shows the MIMO-OFDM transceiver structure.

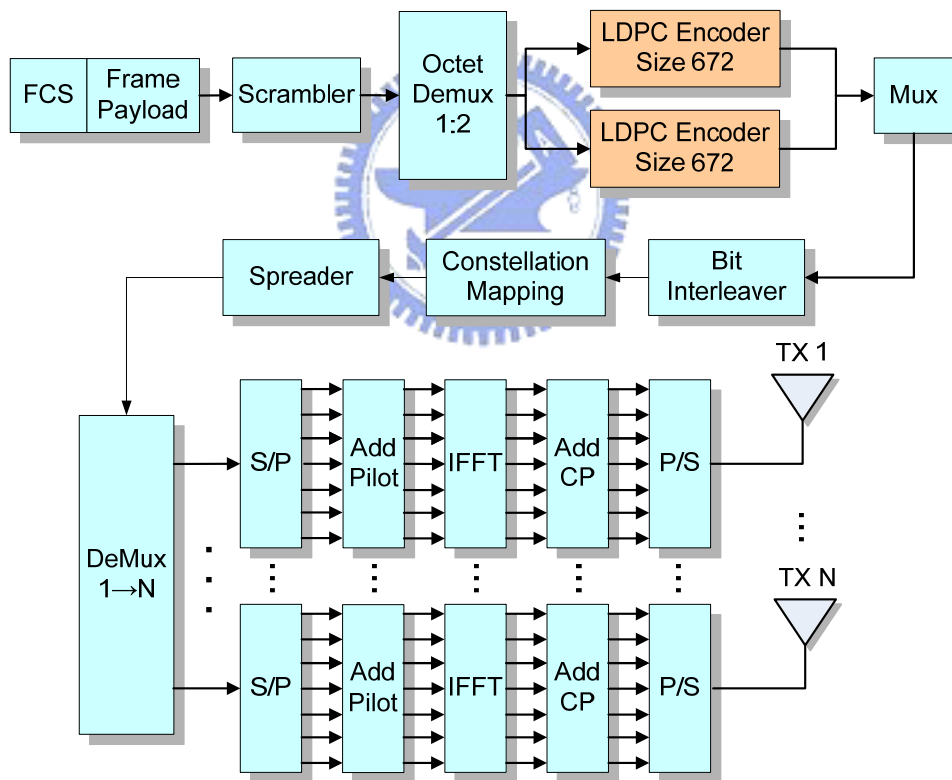


Figure 5-1 MIMO-OFDM transmitter block diagram

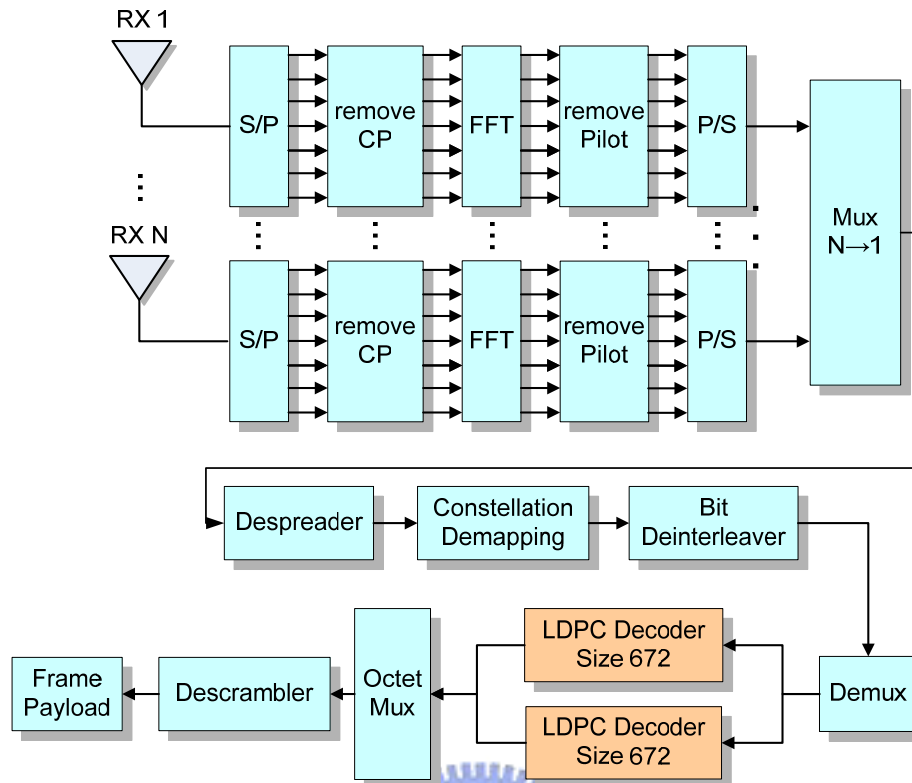


Figure 5-2 MIMO-OFDM receiver block diagram

5.2 MIMO detectors

There exist many signal detection algorithms in MIMO systems. We will describe the zero forcing (ZF) detection, minimum mean-square error (MMSE) detection scheme, VBLAST, and maximum likelihood detection schemes.

5.2.1 Zero Forcing and Minimum Mean-Square Error Detectors

These two methods are simple and popular for retrieving multiple transmitted data streams at the receiver in MIMO systems. The ZF detector is mainly applied to remove the inter-stream interference, completely. The MMSE detector is to minimize the average mean-square error between the transmitted signal and its estimate. In practice, the HSI mode is expected to reach a high data rate, so the system complexity should be kept as simple as possible. Thus, the linear detection schemes such as ZF

and MMSE, which provide a sub-optimal performance but offer significant complexity reduction, are good candidates for the detector, specifically for the system with a large number of transmit and receive antennas. The estimated signal vector can be expressed by

$$\hat{x} = [x_1 \cdots x_M]^T = G \cdot y \quad (5-3)$$

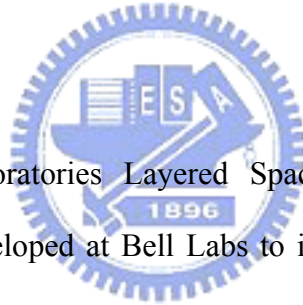
where G is the equalization matrix defined as:

$$\text{ZF equalizer : } G_{ZF} = (H_{ch}^H H_{ch})^{-1} H_{ch}^H \quad (5-4)$$

$$\text{MMSE equalizer : } G_{MMSE} = (H_{ch}^H H_{ch} + \sigma_n^2 I)^{-1} H_{ch}^H \quad (5-5)$$

5.2.2 VBLAST algorithm

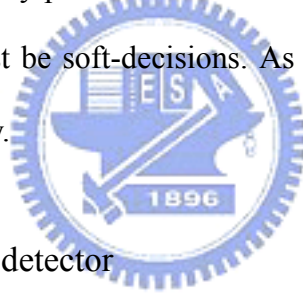
The Vertical Bell Laboratories Layered Space-Time (V-BLAST) detection algorithm was originally developed at Bell Labs to improve the performance of the ZF and MMSE algorithm. This algorithm, which is nonlinear, is based on the ideas of optimal ordering and successive interference cancellation. First, V-BLAST detects a component in the receive signal vector with the largest signal to noise ratio (SNR) and then removes the detected symbol from the received signal vector. For this detection purpose, the ZF or MMSE detector can be used. Then, V-BLAST detects another component with the largest SNR in the residual components. Then, it repeats the process until all symbols are detected. The detection algorithm can be summarized as follows:



$$\begin{aligned}
\text{Initialization } G_1 &= (H_{ch}^H H_{ch})^{-1} H_{ch}^H \quad (\text{for ZF}) \\
&= (H_{ch}^H H_{ch} + \sigma_n^2 I)^{-1} H_{ch}^H \quad (\text{for MMSE}) \\
y_1(k) &= y(k)
\end{aligned}$$

$$\begin{aligned}
\text{recursive } o_n &= \arg \min_{j \in \{o_1 \dots o_{n-1}\}} \|(G_n)_j\|^2 \\
w_{o_n} &= (G_n)_{o_n} \\
z_{o_n}(k) &= w_{o_n}^H y_n(k) \\
\hat{x}_{o_n}(k) &= \text{dec}\{z_{o_n}(k)\} \\
y_{n+1}(k) &= y_n(k) - H_{o_n} \hat{x}_{o_n}(k) \\
G_{n+1} &= (\tilde{H}_{o_n})^H \quad (\tilde{H}_{o_n} : \text{By removing } o_n^{\text{th}} \text{ column of } H) \\
n &= n+1
\end{aligned} \tag{5-6}$$

Note that the V-BLAST can only provide hard-decision outputs. It is known that for a LDPC decoder, the input must be soft-decisions. As a result, the V-BLAST detector cannot be applied here directly.



5.2.3 Maximum Likelihood detector

The optimum detector for a MIMO system is the Maximum Likelihood (ML) detector. The ML detector determines the vector \hat{x}_{ML} minimizing the Euclidean distance between $H\hat{x}_{ML}$ and the received vector y , i.e.,

$$\hat{x} = \arg \min_{x \in S} \|y - Hx\|^2 \tag{5-7}$$

The ML detector solves the above optimization problem with an exhaustive search over the set S which include all possible transmit vectors. As we can image, the computational complexity will be very high when the QAM size is large or the number of transmit and receive antenna is large. Various suboptimum detectors have been proposed in literature [8]-[10]. Also note that the outputs of the ML detector are hard decisions.

A critical operation before the FEC decoding is bit demapping. There are two different demapping schemes, one is hard demapping, and the other is soft demapping. Hard demapping detects bits which are equal to “0” or “1”. Soft demapping gives the probabilities of being equal to “0” or “1”. The ML detector we mention in the previous paragraph is a hard demapping scheme. For the purpose of LDPC decoding, we want to use a soft demapping scheme.

In soft demapping, Log-Likelihood Ratio (LLR) is a commonly used variable to present soft output information. Let y denote the received signal vector, x the transmit signal vector, and $b_{N,k}$ be the k^{th} bit of its N^{th} component. The optimum hard decision on bit $b_{N,k}$ is given by the rule

$$\hat{b}_{N,k} = \beta \quad \text{if } P[b_{N,k} = \beta | y] > P[b_{N,k} = (1 - \beta) | y] \quad , \beta = 0,1 \quad (5-8)$$

Set $\beta = 1$, then (5-8) can be rewritten as

$$\hat{b}_{N,k} = 1 \quad \text{if } \log \frac{P[b_{N,k} = 1 | y]}{P[b_{N,k} = 0 | y]} > 0 \quad (5-9)$$

Thus, the Log-Likelihood Ratio (LLR) of decision bit $\hat{b}_{N,k}$ is defined as

$$\begin{aligned} LLR(b_{N,k}) &= \log \frac{P[b_{N,k} = 1 | y]}{P[b_{N,k} = 0 | y]} \\ &= \log \frac{\sum_{\alpha_1 \in S_{N,k}^{(1)}} P[x = \alpha_1 | y]}{\sum_{\alpha_0 \in S_{N,k}^{(0)}} P[x = \alpha_0 | y]} \end{aligned} \quad (5-10)$$

where $S_{N,k}^{(1)}$ denote a set including all the symbols with $b_{N,k} = 1$, and $S_{N,k}^{(0)}$ which is its complementary.

Applying the Bayes rule and assuming that the transmitted symbols have equal probability, we can rewrite (5-10) as

$$LLR(b_{N,k}) = \log \frac{\sum_{\alpha_1 \in S_{N,k}^{(1)}} P(y | x = \alpha_1)}{\sum_{\alpha_0 \in S_{N,k}^{(0)}} P(y | x = \alpha_0)} \quad (5-11)$$

If the noise is Gaussian distributed, the summation of exponentials involved in (5-11)

can be approximated according to the following so called the max-log approximation

$$LLR(b_{N,k}) = \log \frac{\max_{\alpha_1 \in S_{N,k}^{(1)}} P(y | x = \alpha_1)}{\max_{\alpha_0 \in S_{N,k}^{(0)}} P(y | x = \alpha_0)} \quad (5-12)$$

Since y is complex Gaussian distributed, we have

$$P(y | x = \alpha) = \frac{1}{\sqrt{2\pi\sigma}} \exp \left\{ -\frac{1}{2} \frac{\|y - Hx\|^2}{\sigma^2} \right\} \quad (5-13)$$

Using (5-12) and (5-13), we can have

$$LLR(b_{N,k}) = \frac{1}{2\sigma^2} \left\{ \min_{x \in S_{N,k}^{(1)}} \|y - Hx\|^2 - \min_{x \in S_{N,k}^{(0)}} \|y - Hx\|^2 \right\} \quad (5-14)$$

From $S_{N,k}^{(1)}$ and $S_{N,k}^{(0)}$ these two set, we can search the symbol which can minimize the Euclidean distance from y to Hx . The difference of these two minimized distance

is the LLR we want to estimate. The factor $\frac{1}{2\sigma^2}$ can be viewed as a weighted factor.


Similar to the ML detector, the MIMO demapping algorithm requires high computational complexity. Many suboptimum algorithms have been proposed to solve the problem [11]-[12].

Chapter 6 Simulations

In this Chapter, we will report our simulation results in two parts. One is the performance of SISO system based on IEEE 802.15.3c transmitter specification and the receiver we designed. And the second part is the simulation result for the SDMA system.

Part 1 IEEE 802.15.3c SISO system performance comparison

The HSI PHY modulation and coding scheme is listed in Table 6-1. For the FEC rates of 1/2, 5/8, 3/4 and 7/8, LDPC(672,336), LDPC(672,504), LDPC(672,420) and LDPC(672,588) codes are used respectively.



MCS index	Data rate (Mb/s)	Modulation scheme	Spreading factor (L_f)	Coding mode	FEC rate (R_{FEC})
1	1512	QPSK	1	EEP	1/2
2	2268	QPSK	1		3/4
3	2646	QPSK	1		7/8
4	3024	16-QAM	1		1/2
5	4536	16-QAM	1		3/4
6	5292	16-QAM	1		7/8
7	5670	64-QAM	1		5/8

Table 6-1 HSI PHY MCS dependent parameters

We consider a SISO system with these modulation and coding schemes as shown in Table 6-1. Two channel models are considered. The first one is the AWGN channel and the other is multi-path Rayleigh fading channel.

The number of iterations for the LDPC code is critical. The higher the numbers, the better performance we will have. However, the computational complexity will

grow along with the number of the iterations. We then compare the performance for LDPC codes with different numbers of iterations in each modulation and coding schemes. Figure 6-1 to Figure 6-7 show the simulation results for the AWGN channel, and Figure 6-8 to Figure 6-14 show the simulation results for the multi-path Rayleigh fading channel. Here, we let the inner receiver be ideal. In other words, there are not synchronization or channel estimation errors. From the figures, we can find that the performance of the LDPC code have a convergent tendency. There is a tradeoff that can be considered between the system complexity and performance.

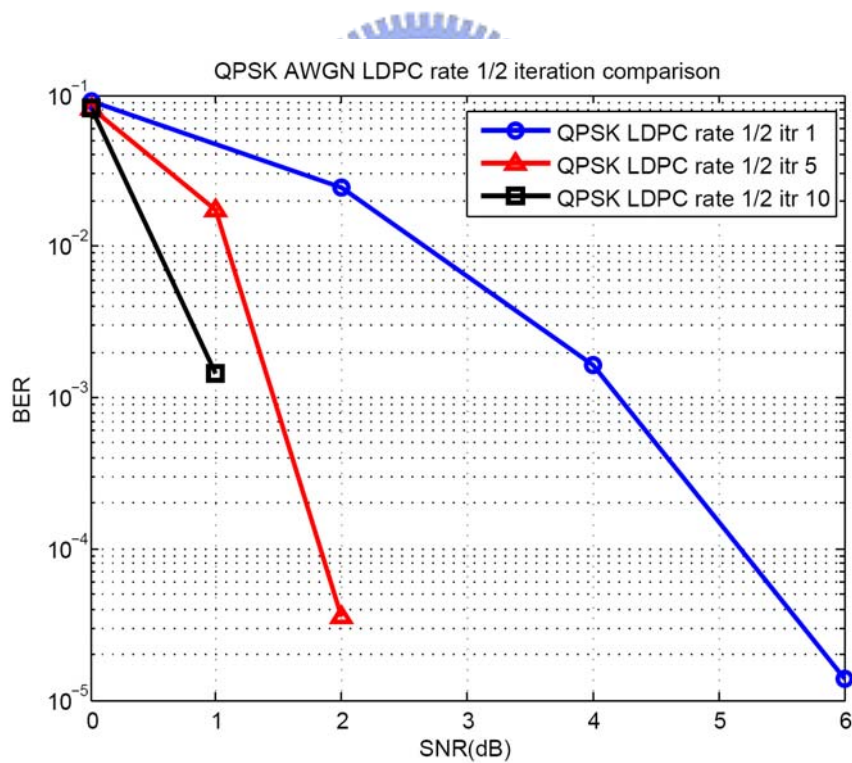


Figure 6-1 BER comparison of LDPC iteration for coding rate 1/2 in QPSK AWGN channel

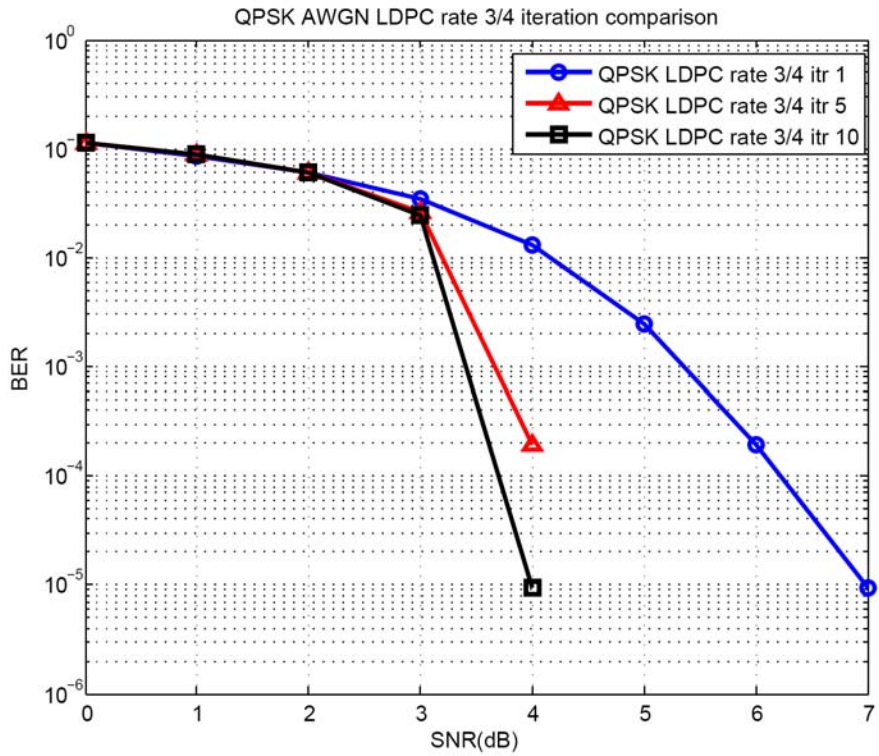


Figure 6-2 BER comparison of LDPC iteration for coding rate 3/4 in QPSK AWGN channel

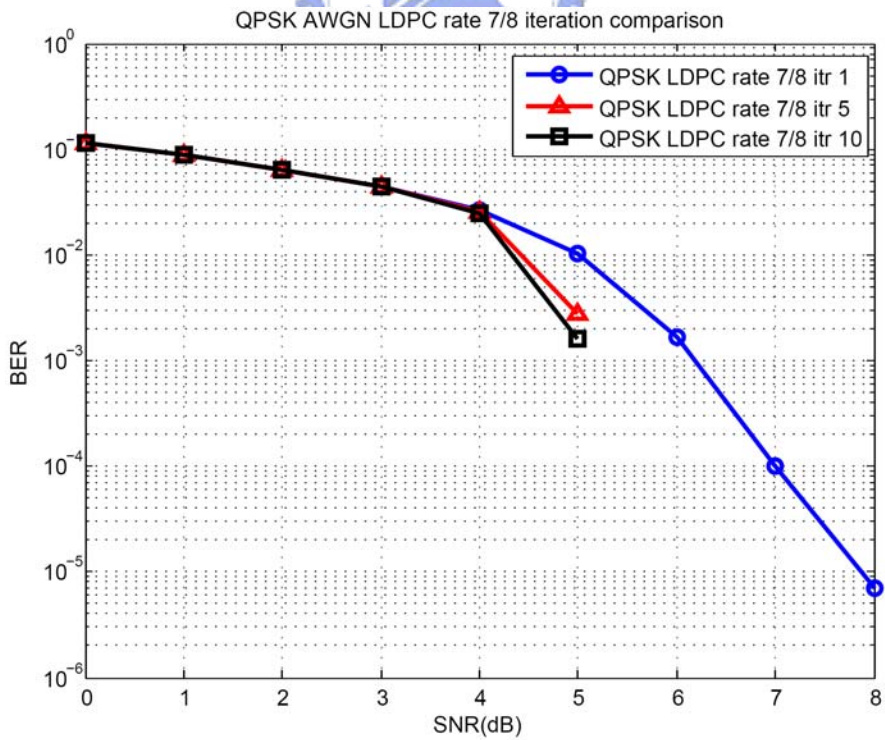


Figure 6-3 BER comparison of LDPC iteration for coding rate 7/8 in QPSK AWGN channel

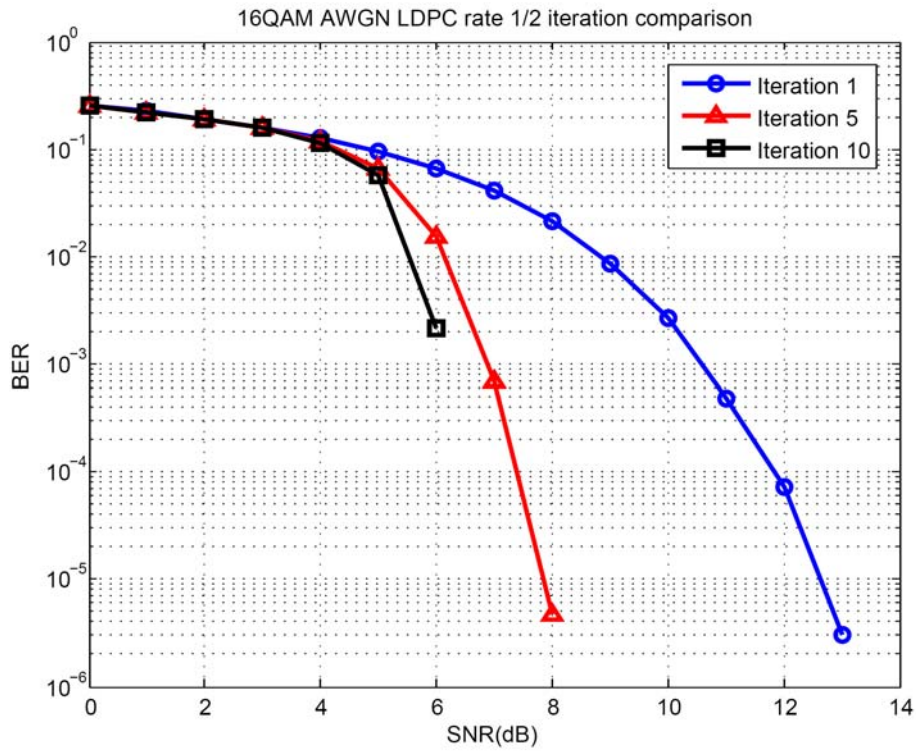


Figure 6-4 BER comparison of LDPC iteration for coding rate 1/2 in 16QAM AWGN channel

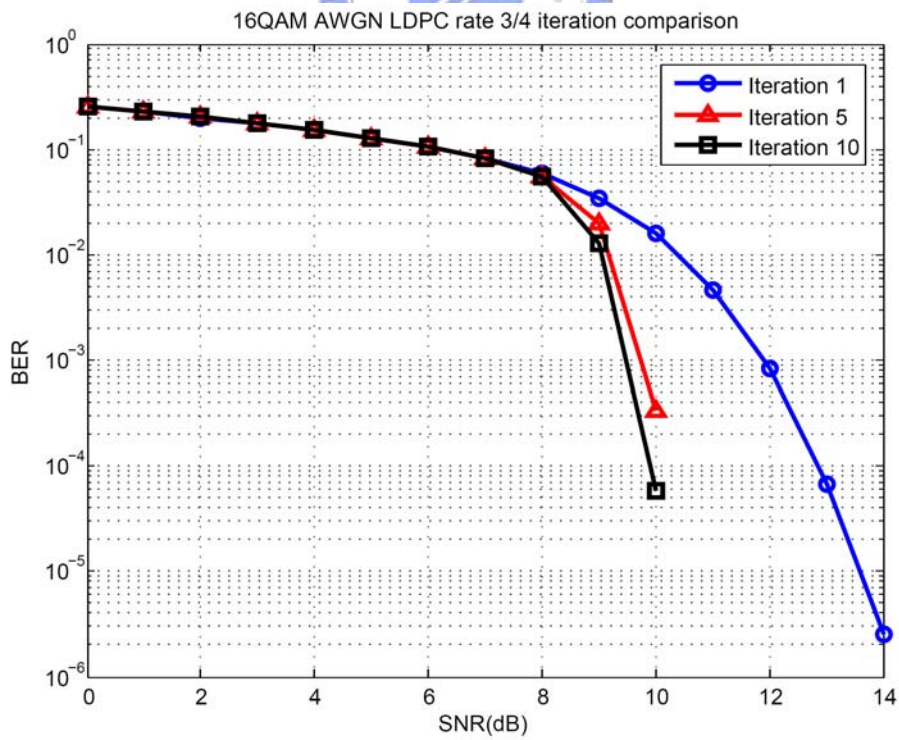


Figure 6-5 BER comparison of LDPC iteration for coding rate 3/4 in 16QAM AWGN channel

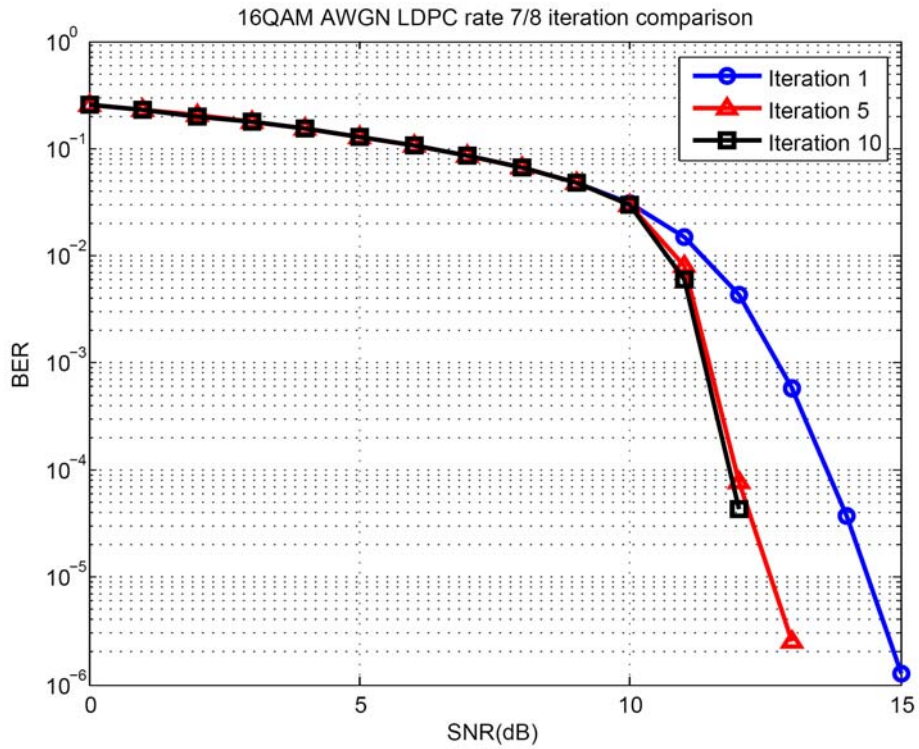


Figure 6-6 BER comparison of LDPC iteration for coding rate 7/8 in 16QAM AWGN channel

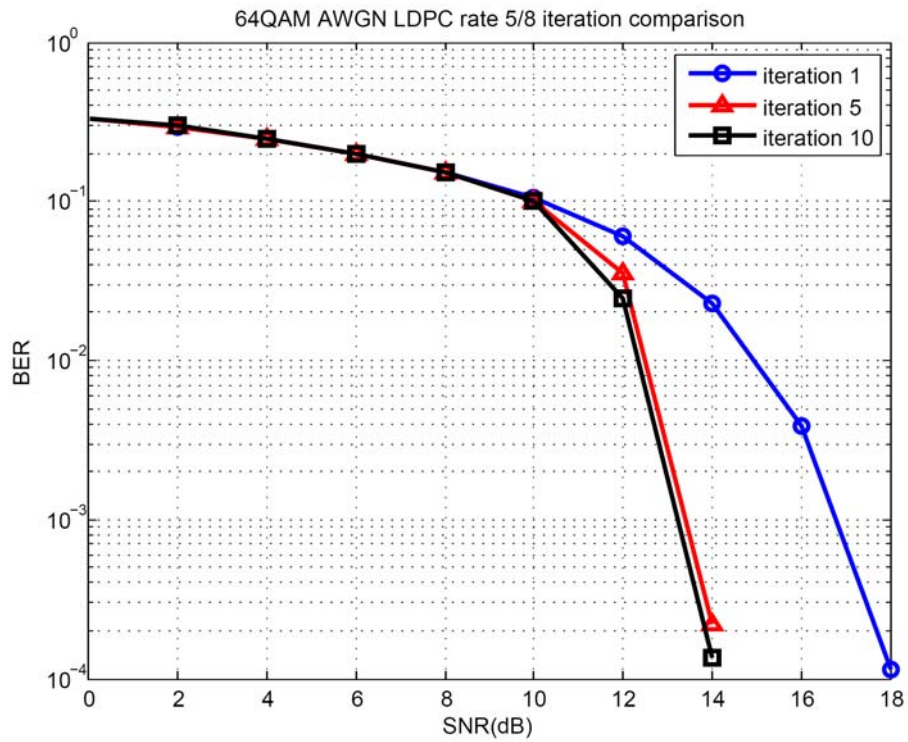


Figure 6-7 BER comparison of LDPC iteration for coding rate 5/8 in 64QAM AWGN channel

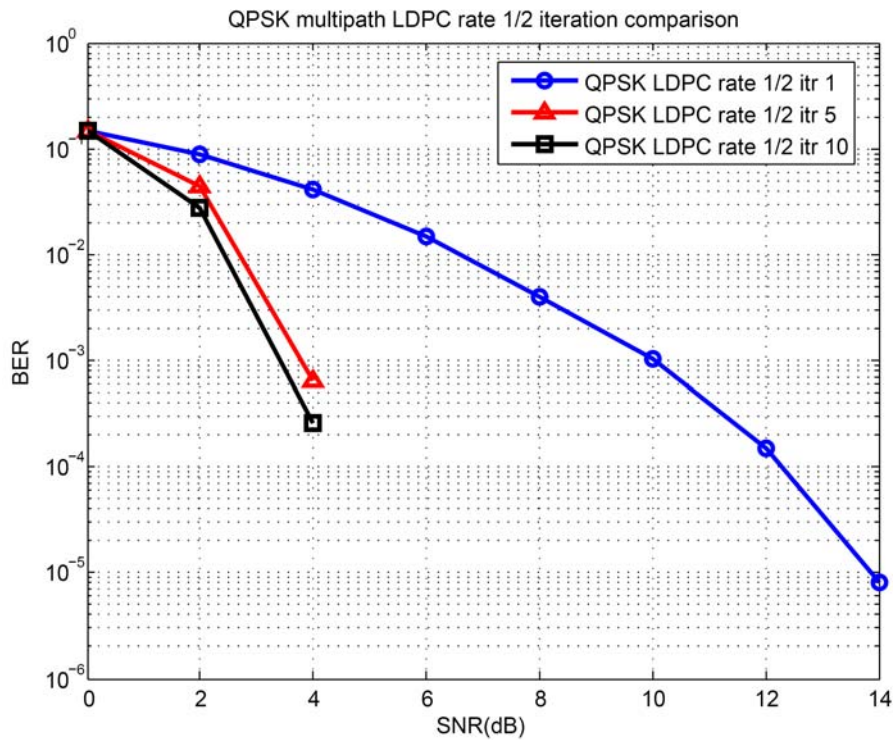


Figure 6-8 BER comparison of LDPC iteration for coding rate 1/2 in QPSK multipath Rayleigh fading channel

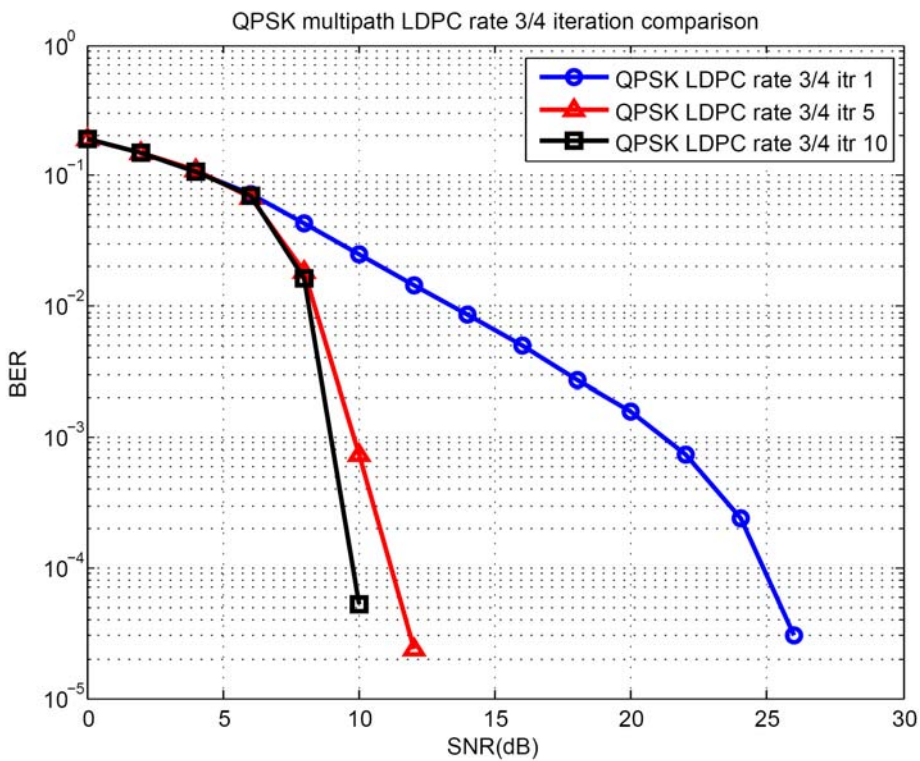


Figure 6-9 BER comparison of LDPC iteration for coding rate 3/4 in QPSK multipath Rayleigh fading channel

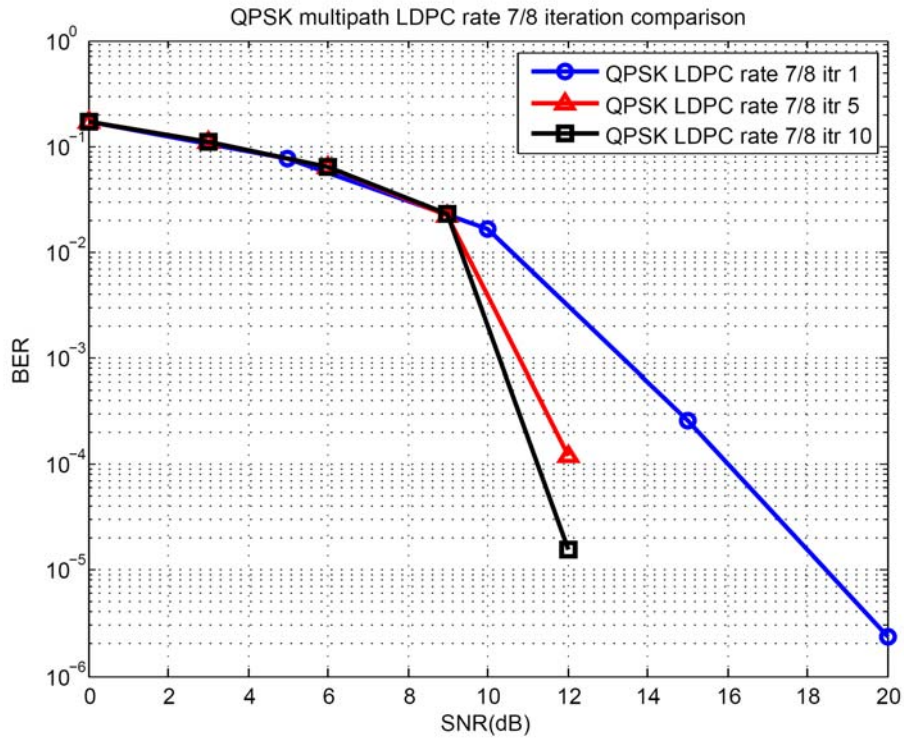


Figure 6-10 BER comparison of LDPC iteration for coding rate 7/8 in QPSK multipath Rayleigh fading channel

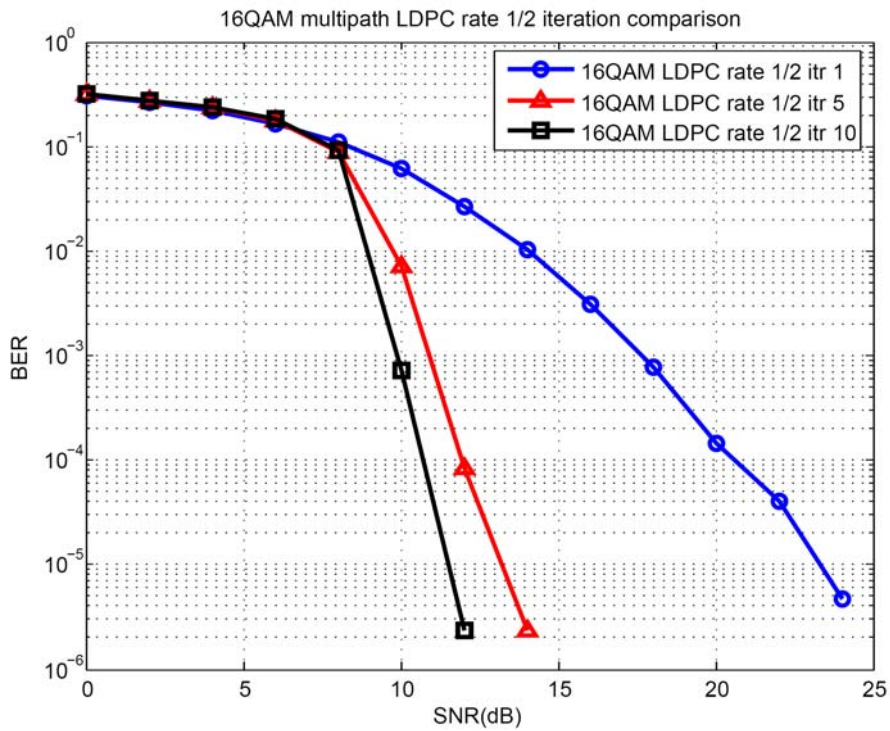


Figure 6-11 BER comparison of LDPC iteration for coding rate 1/2 in 16QAM multipath Rayleigh fading channel

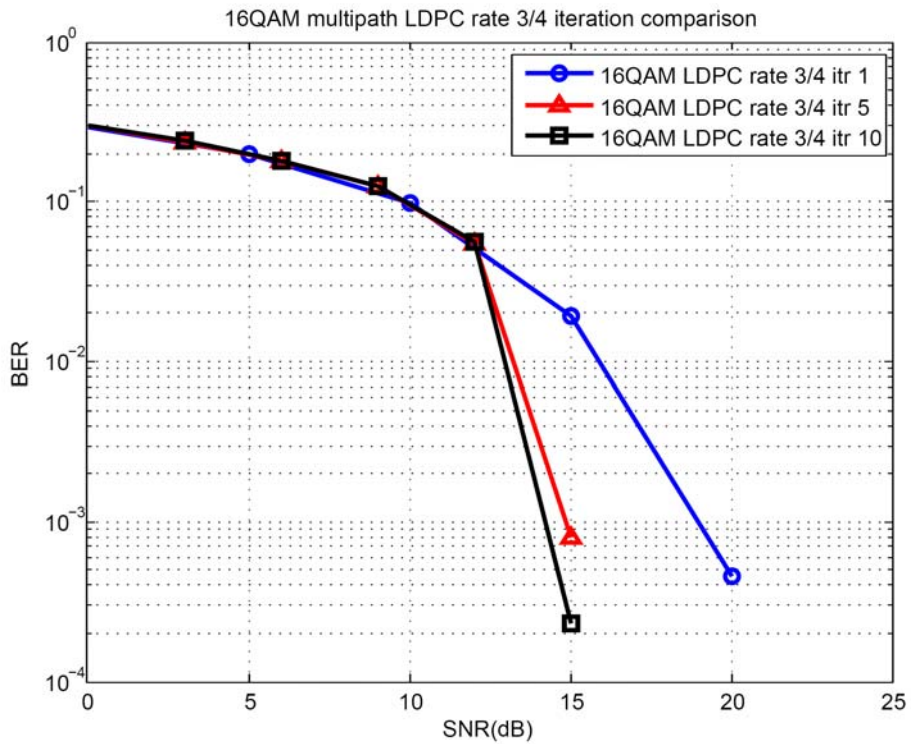


Figure 6-12 BER comparison of LDPC iteration for coding rate 3/4 in 16QAM multipath Rayleigh fading channel

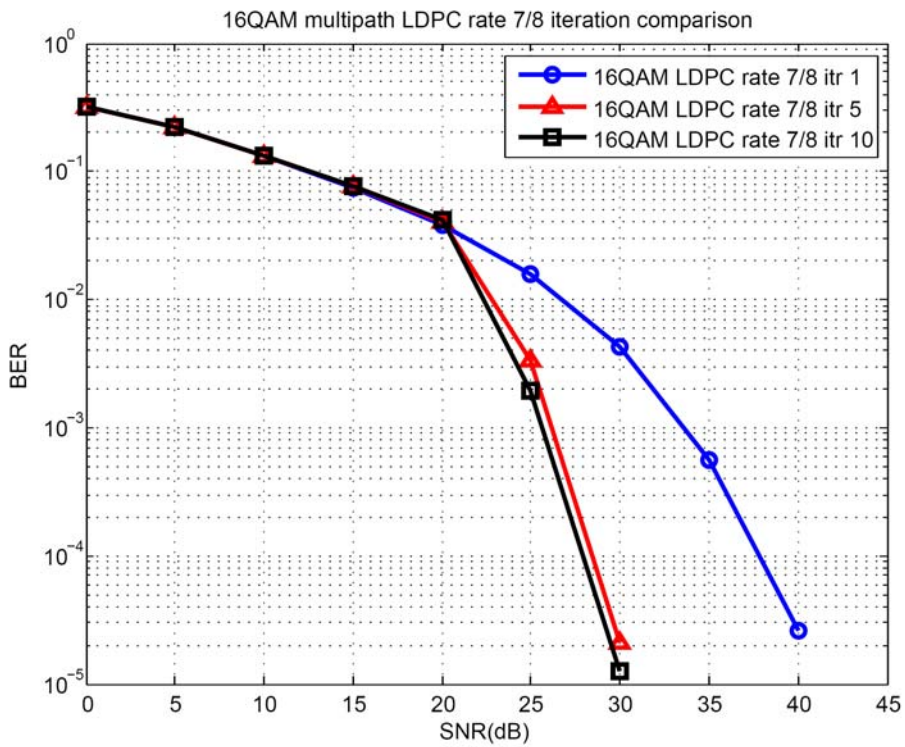


Figure 6-13 BER comparison of LDPC iteration for coding rate 7/8 in 16QAM multipath Rayleigh fading channel

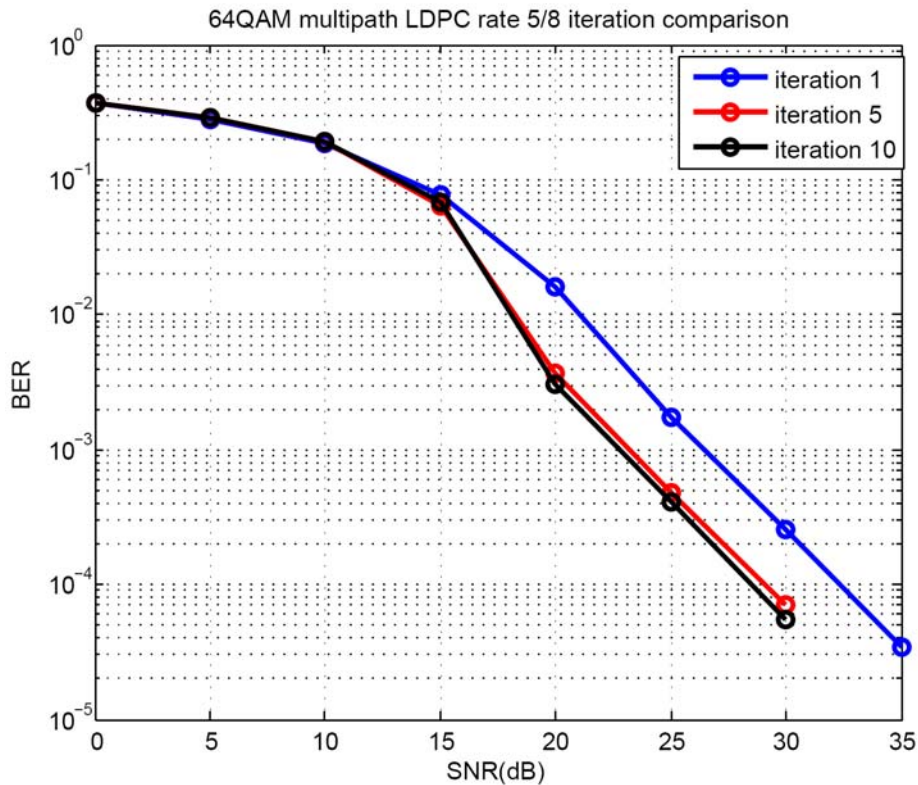


Figure 6-14 BER comparison of LDPC iteration for coding rate 5/8 in 64QAM multipath Rayleigh fading channel

Next, we compare the simulation results between the ideal and real-world conditions. In the ideal condition, there are not synchronization or channel estimation errors and the operation of the inner receiver is bypassed (same as that in Figs 6-8 to 6-14). In the real-world condition, the inner receiver is activated to conduct timing acquisition, synchronization, and channel estimation. Also, we set the number of iteration in the LDPC decoder as 5.

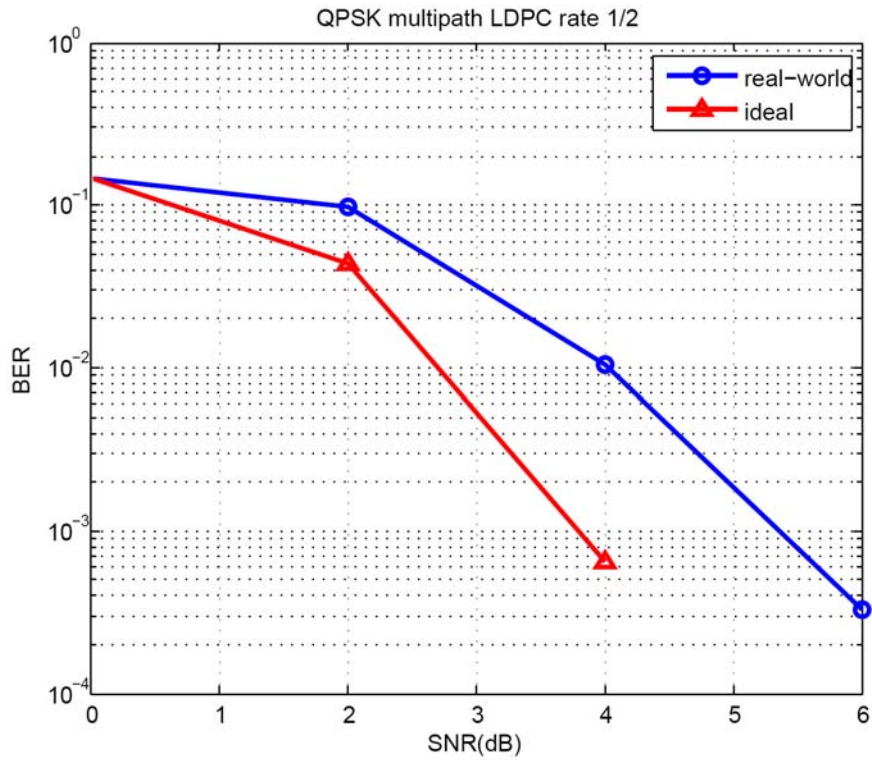


Figure 6-15 Comparison of ideal and real-world condition for coding rate 1/2 in QPSK multipath Rayleigh fading channel

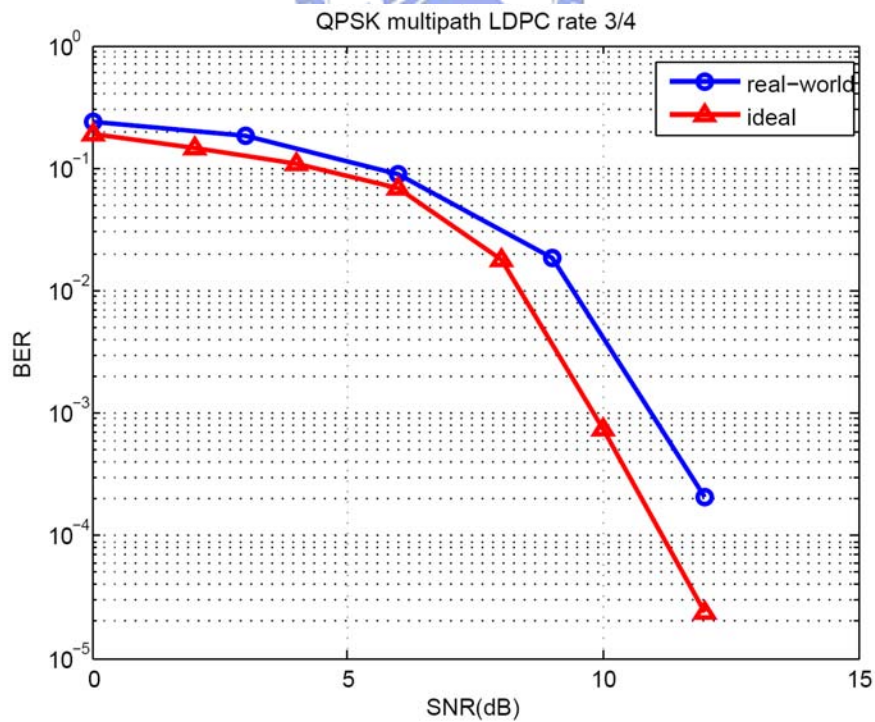


Figure 6-16 Comparison of ideal and real-world condition for coding rate 3/4 in QPSK multipath Rayleigh fading channel

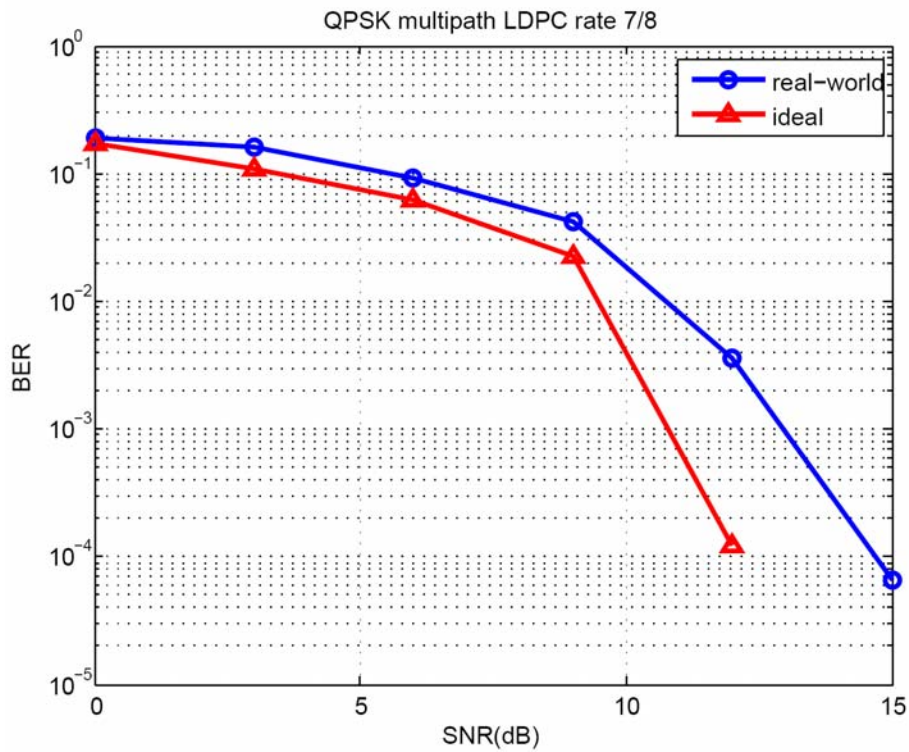


Figure 6-17 Comparison of ideal and real-world condition for coding rate 7/8 in QPSK multipath Rayleigh fading channel

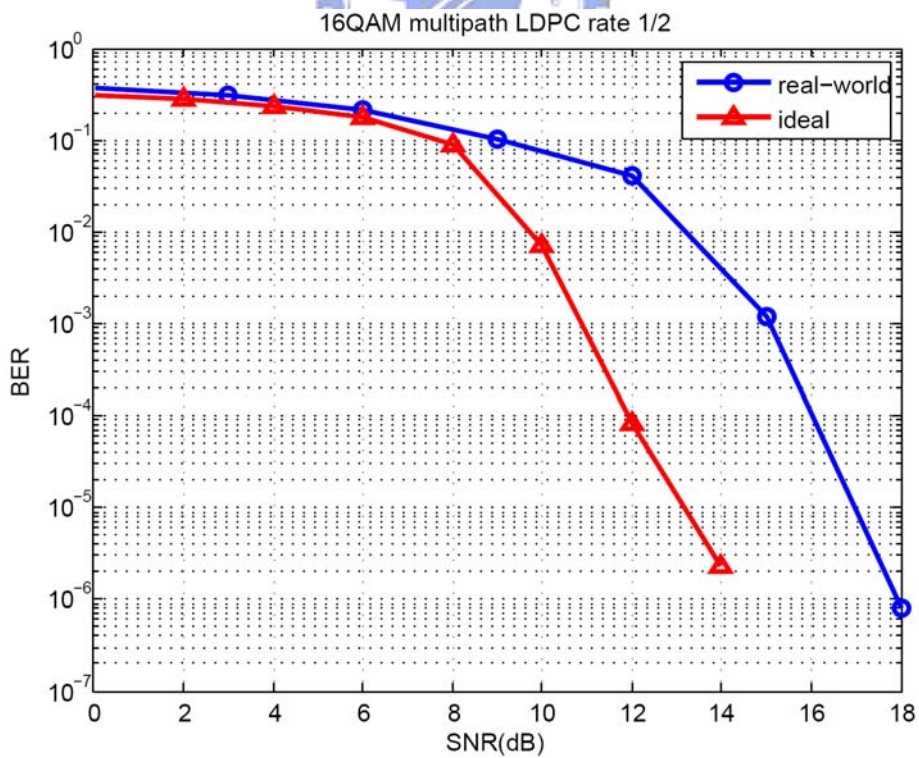


Figure 6-18 Comparison of ideal and real-world condition for coding rate 1/2 in 16QAM multipath Rayleigh fading channel

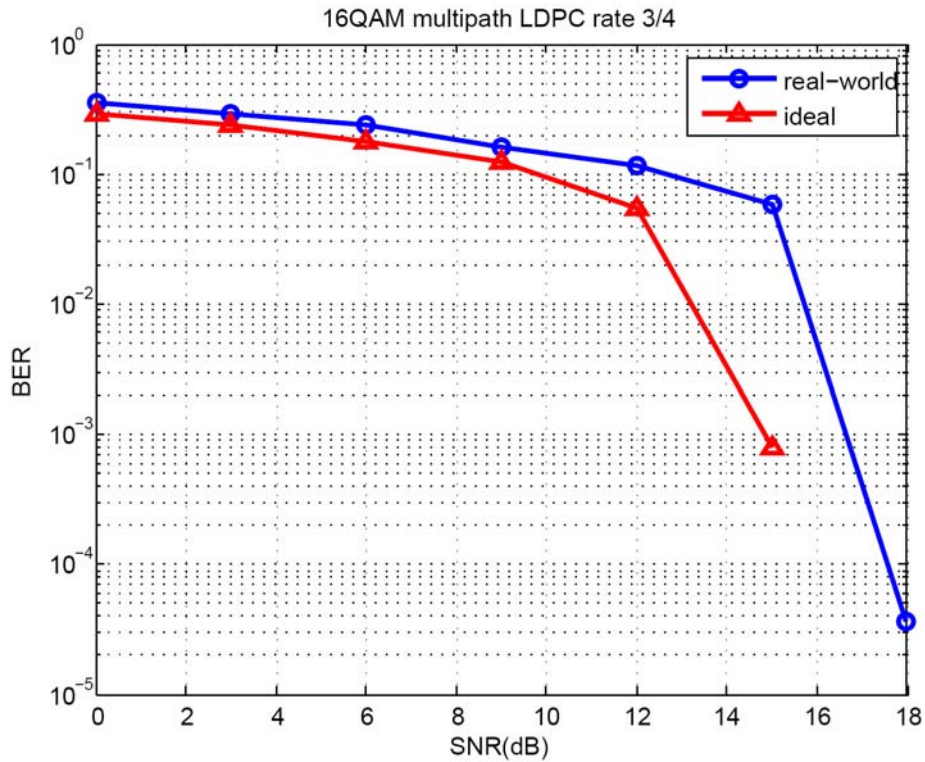


Figure 6-19 Comparison of ideal and real-world condition for coding rate 3/4

in 16QAM multipath Rayleigh fading channel

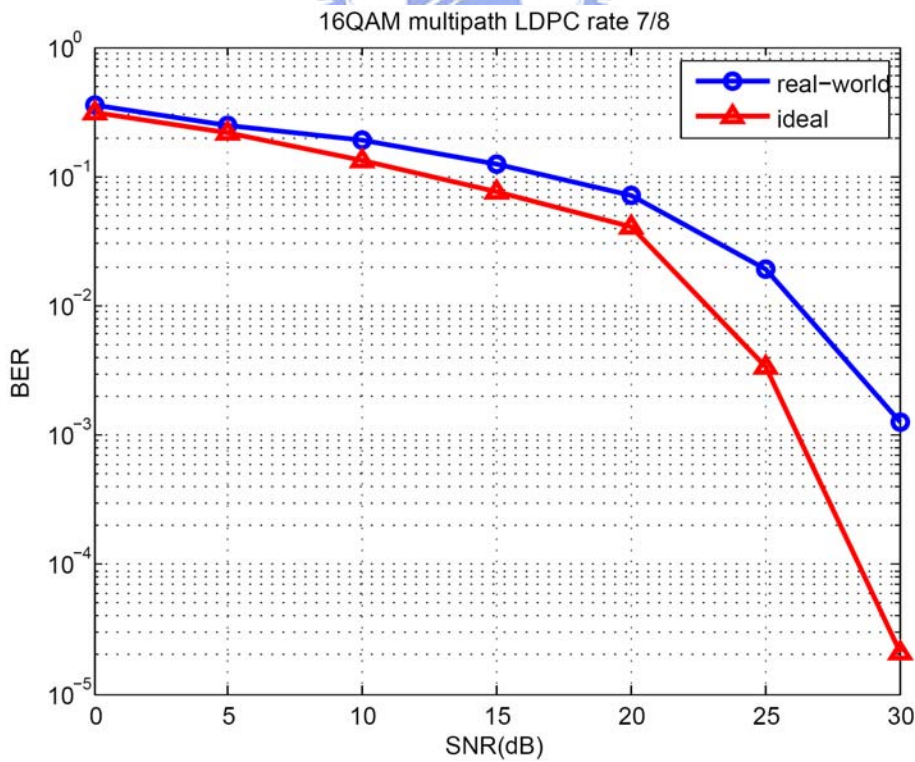


Figure 6-20 Comparison of ideal and real-world condition for coding rate 7/8

in 16QAM multipath Rayleigh fading channel

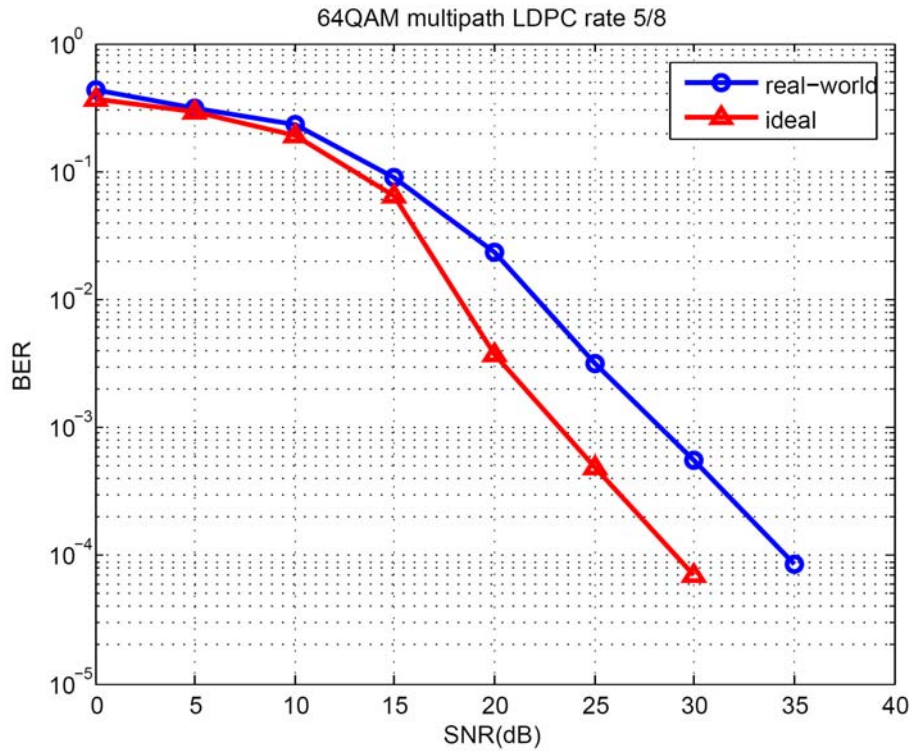


Figure 6-21 Comparison of ideal and real-world condition for coding rate 5/8 in 64QAM multipath Rayleigh fading channel



Part 2 SDMA system in IEEE 802.15.3c

First, we show, by examples, that the digital beamforming algorithm can completely null the interference from the other user. By using the algorithm we mentioned in Chapter 4, we can have the beam pattern as

I. Configuration 1

User 1 $\phi = \pi/4, \theta = \pi/4$

User 2 $\phi = -\pi/4, \theta = \pi/4$ (suppose user 2 is interference)

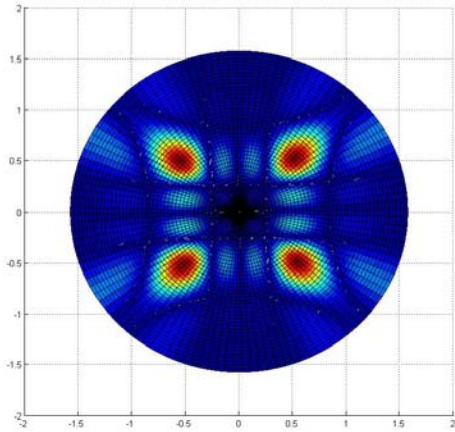


Figure 6-22 Analog beam pattern I

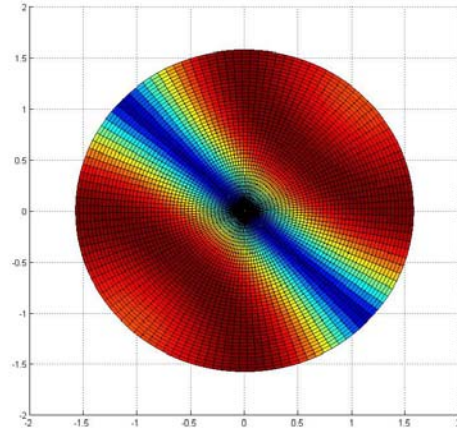


Figure6-23 Digital beam pattern I

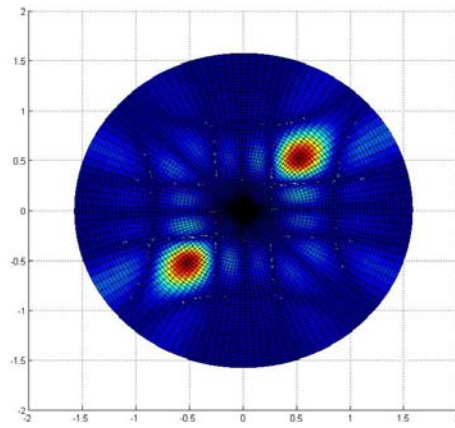


Figure6-24 Hybrid beam pattern I

In Configuration 1, we have only two weights per user.

II. Configuration 2

User 1 $\phi = \pi/4$, $\theta = \pi/4$

User 2 $\phi = -\pi/4$, $\theta = \pi/4$, suppose user 2 is interference

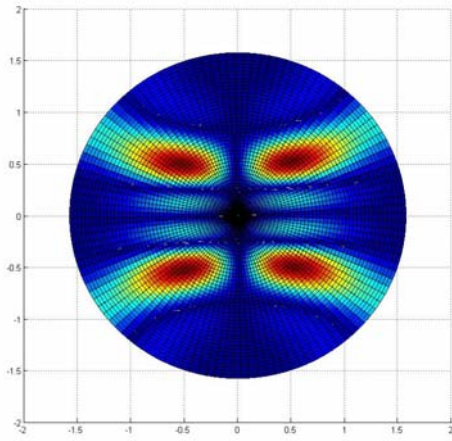


Figure 6-25 Analog beam pattern II

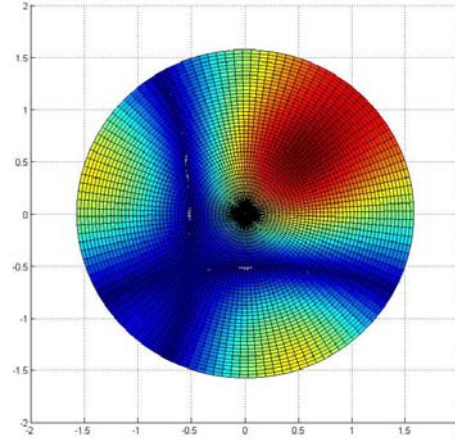


Figure 6-26 Digital beam pattern II

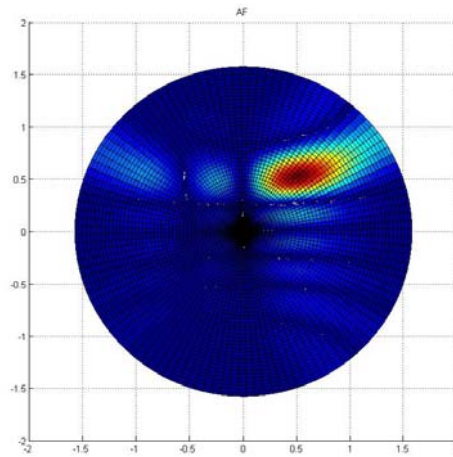


Figure 6-27 Hybrid beam pattern II

In Configuration 2, we have four weights per user. As we can see from the above example, the interference from the other direction is nulled completely.

According to Chapter 4-3, we can then model this SDMA system as a MIMO system. Assume that the channel is an AWGN channel, and two transmitter antennas and two receiver antennas are used (two users). The power gains corresponding to different pointing angles using analog beamforming are listed below:

User1	User2	Main power gain	Interference power gain	angle
45°	44°	0.4817	0.4793	1°
45°	43°	0.4817	0.4721	2°

45°	42°	0.4817	0.4602	3°
45°	40°	0.4817	0.423	5°
45°	37°	0.4817	0.34	8°
45°	35°	0.4817	0.2740	10°
45°	30°	0.4817	0.1148	15°
45°	-15°	0.4817	0.0035	60°
45°	-45°	0.4817	0	90°
45°	-135°	0.4817	0	180°

Table 6-2 Power gain with different angles using analog beamforming

Figure 6-21 to Figure 6-25 shows the performance of the SDMA system with analog beamforming (IEEE 802.15.3c). Here, the QPSK modulation scheme is used at the transmitter and the MIMO detector is used at the receiver, including the ML, VBLAST MMSE, VBLAST ZF, MMSE and ZF detectors.

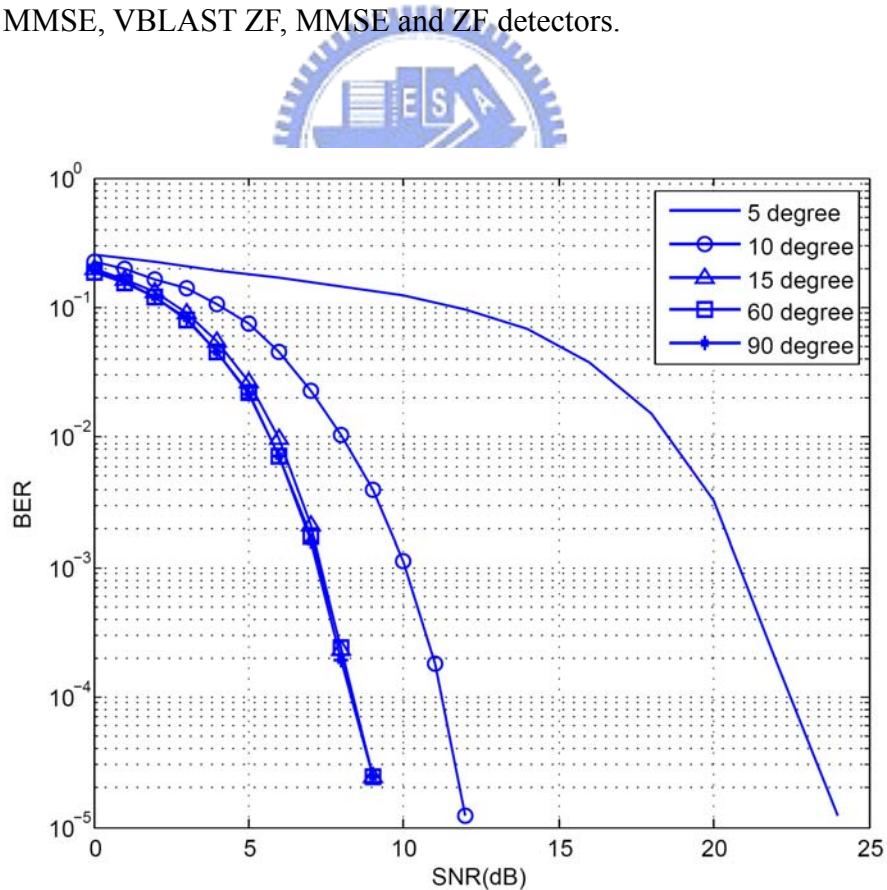


Figure 6-28 Performance of SDMA system with analog beamforming using ML detector (IEEE 802.15.3c)

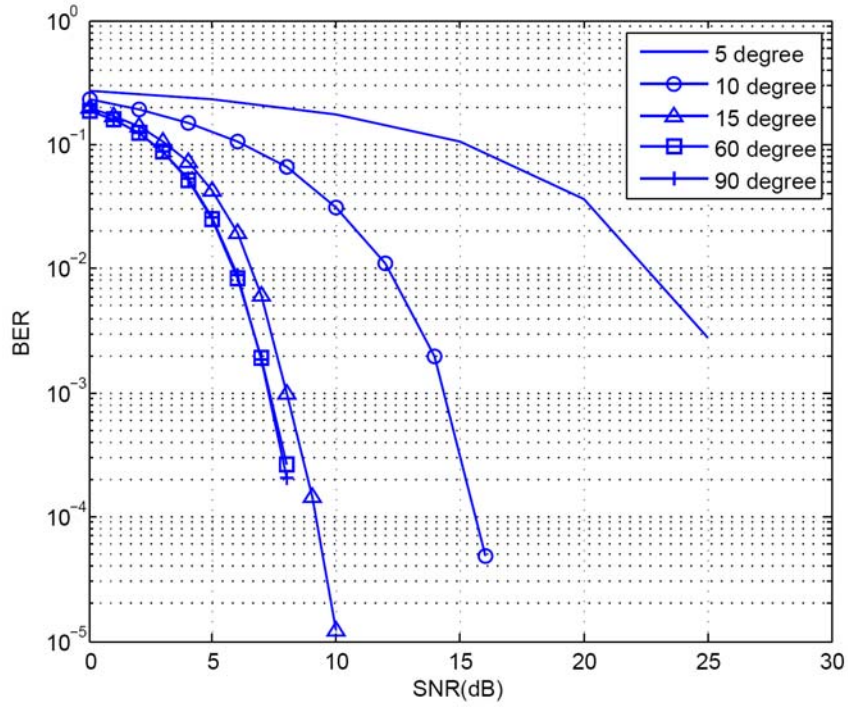


Figure 6-29 Performance of SDMA system with analog beamforming using VBLAST MMSE detector (IEEE 802.15.3c)

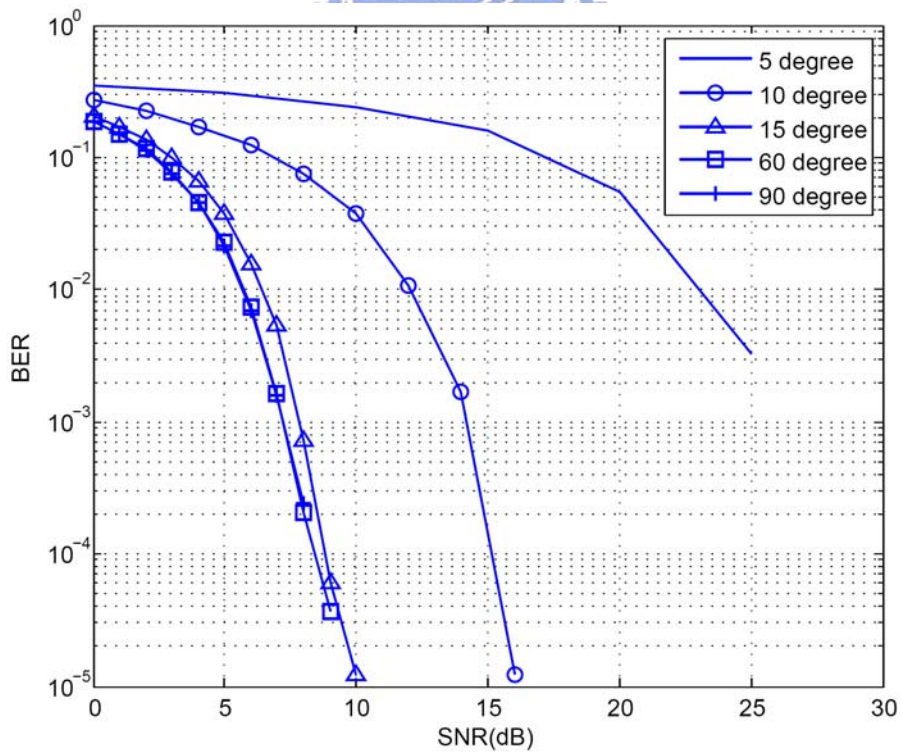


Figure 6-30 Performance of SDMA system with analog beamforming using VBLAST ZF detector (IEEE 802.15.3c)

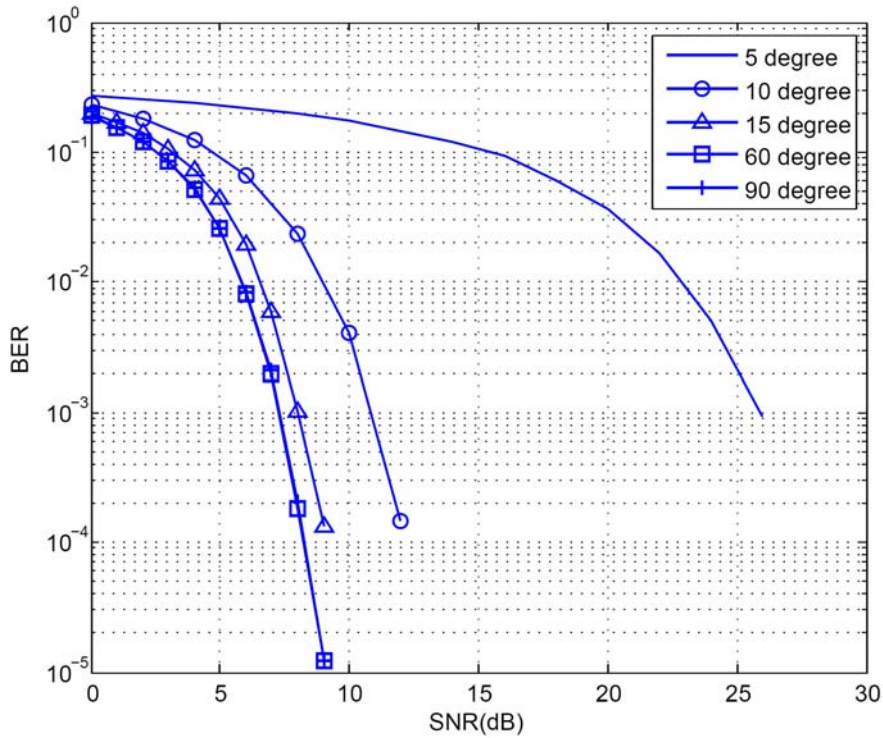


Figure 6-31 Performance of SDMA system with analog beamforming using MMSE detector (IEEE 802.15.3c)

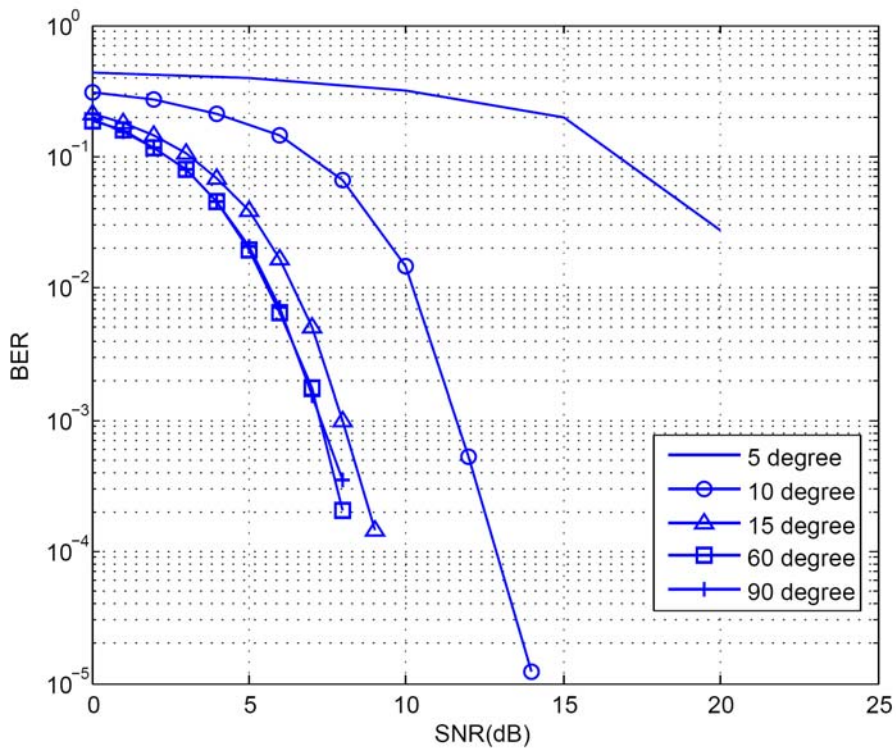


Figure 6-32 Performance of SDMA system with analog beamforming using ZF detector (IEEE 802.15.3c)

We can find that the system can have good performance in each detector when the angle separation of the two users is larger than 15 degree.

Figure 6-26 to Figure 6-30 re-compile the results in Figure 6-21 to 6-25 and show the performance comparison for the case 90°, 60°, 15°, 10°, and 5°. We can find that if the angle is larger then 15°, the performance is almost the same between these detectors. It is because the interference is small and there is no performance gain with advanced algorithms. On the other hand, if the angle is smaller than 15°, we can find that the ML detector is better than other detectors.

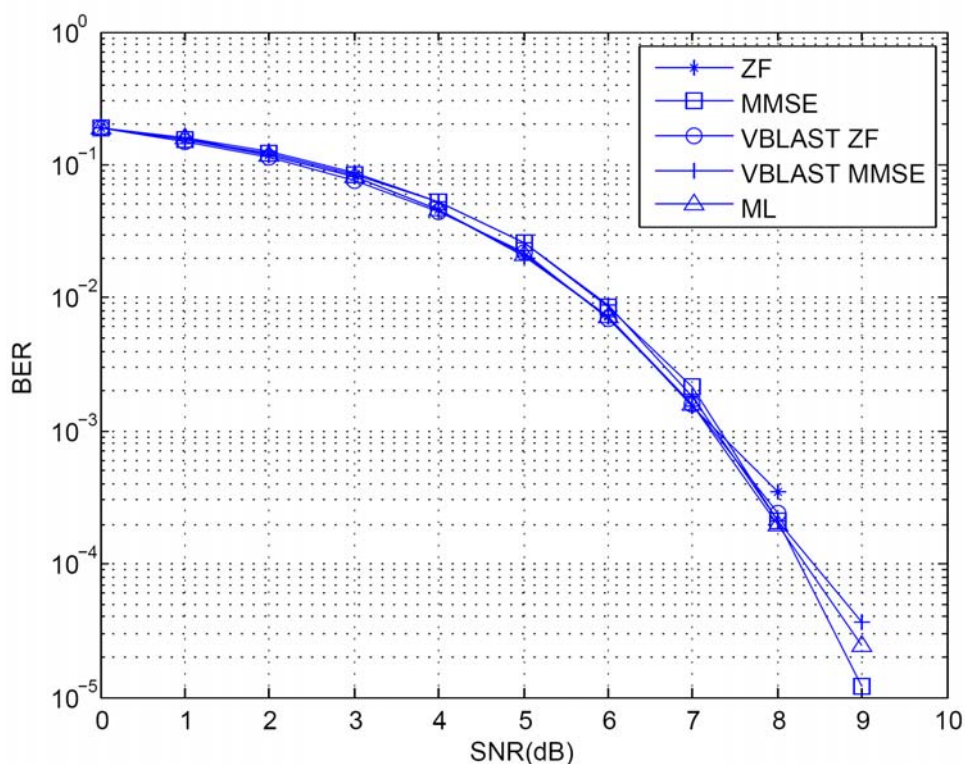


Figure 6-33 Performance of analog beamforming comparison with angle 90°

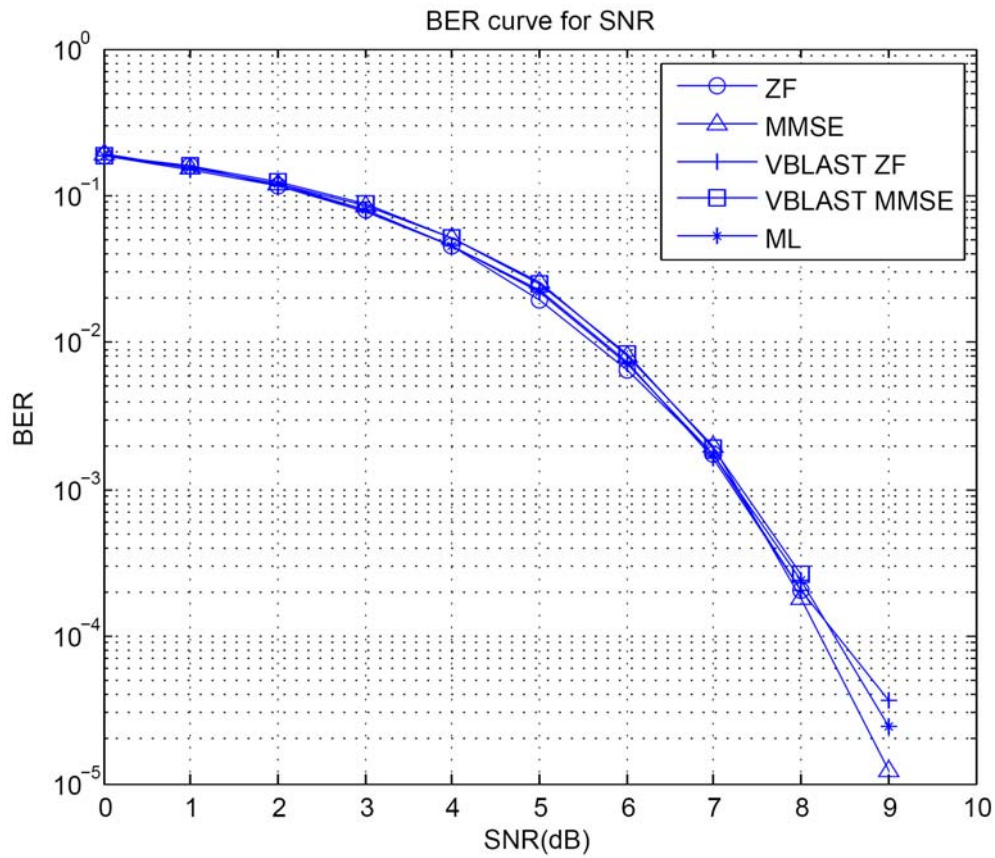


Figure 6-34 Performance of analog beamforming comparison with angle 60°

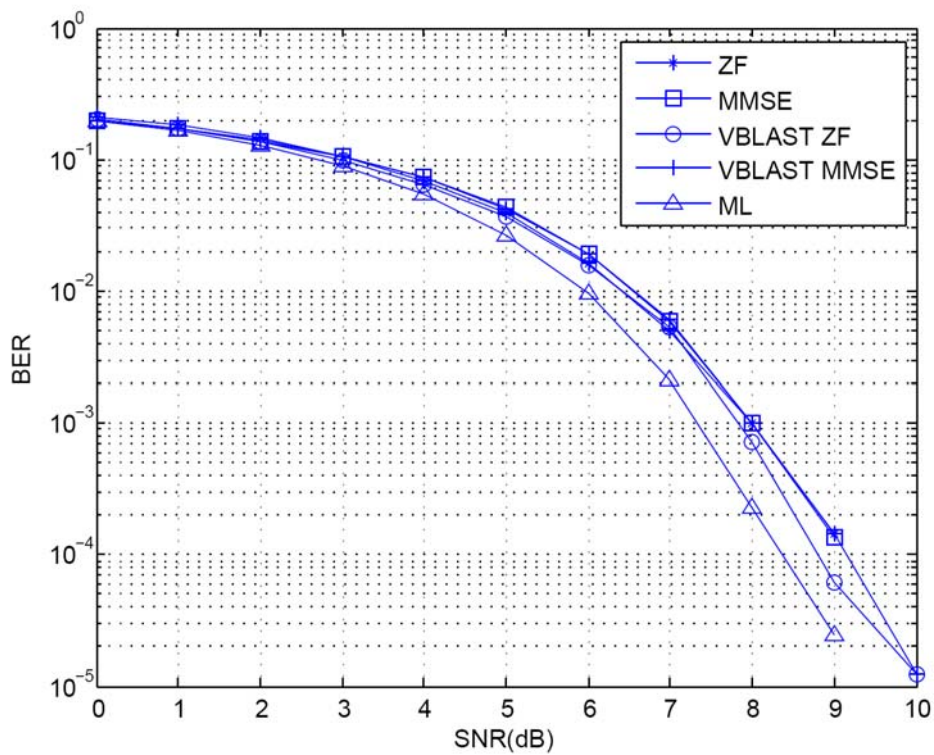


Figure 6-35 Performance of analog beamforming comparison with angle 15°

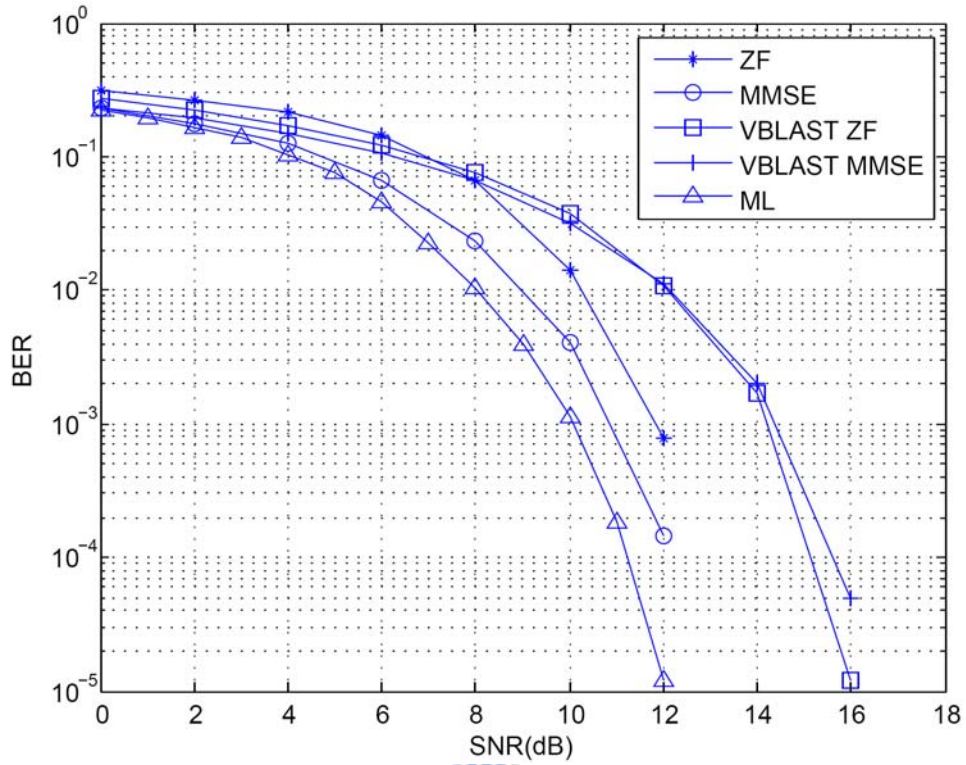


Figure 6-36 Performance of analog beamforming comparison with angle 10°

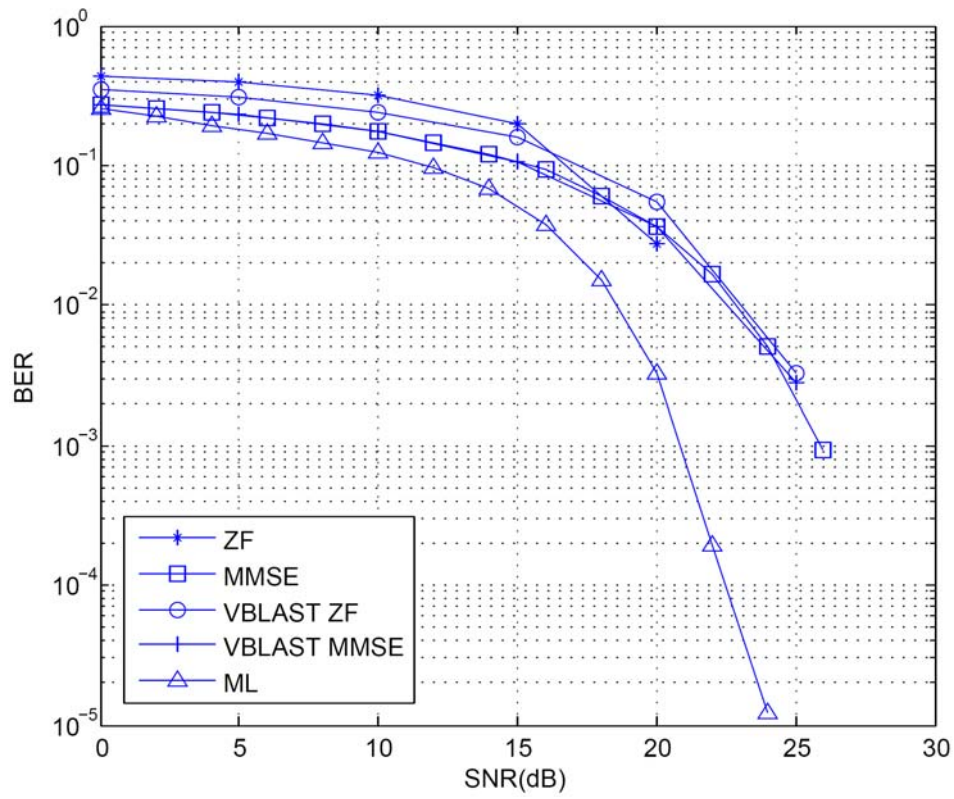


Figure 6-37 Performance of analog beamforming comparison with angle 5°

The power gains corresponding to different pointing angles using digital beamforming are listed below:

User1	User2	Main power gain	Interference power gain	angle
45°	44°	0.0003541	0	1°
45°	43°	0.0014	0	2°
45°	42°	0.0031	0	3°
45°	40°	0.0081	0	5°
45°	37°	0.0195	0	8°
45°	35°	0.0291	0	10°
45°	30°	0.059	0	15°
45°	-15°	0.3889	0	60°
45°	-45°	0.4817	0	90°
45°	-135°	0.4817	0	180°

Table 6-3 Power gain with different angles using hybrid beamforming

Figure 6-31 shows the performance with hybrid beamforming in using ML detector. Note that in hybrid beamforming, although the interference can be perfectly nulled, the power in the desired beam is reduced significantly. If we assume that the main power and interference power are the same before beamforming, we can find the BER performance in Figure 6-26 is worse than that of analog beamforming in Figure 6-21. The result can be explained by the fact that the cost function to minimize in (4-11) is the interference power. However, the signal-to-interference-plus-noise-ratio (SINR), not the interference power, is the factor determining the final performance. As a result, while the interference power may be reduced to the minimum, the SINR may also be reduced. In other words, if we can use the SINR as the criterion when designing the hybrid beamformer, the performance can be enhanced. We can expect that the performance of hybrid beamforming should be better than analog beamforming.

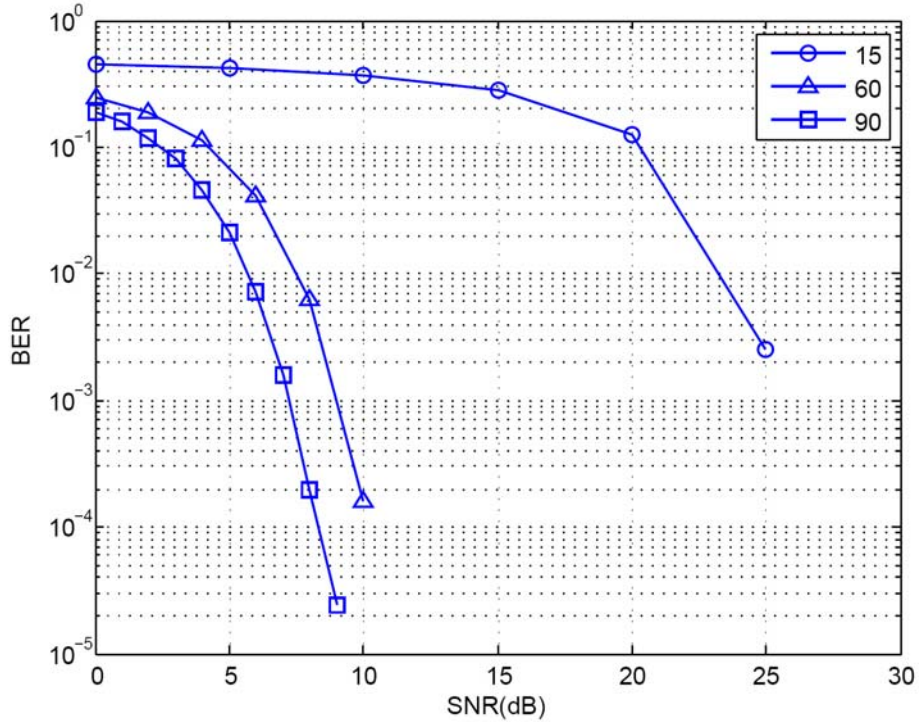


Figure 6-38 Performance of SDMA system with hybrid beamforming using ML detector (IEEE 802.15.3c)

Chapter 7 Conclusions

7.1 Conclusions

Over Gbps wireless transmission in unlicensed 60GHz band has drawn considerably attention recently. The IEEE has formed a task force, referred to as 802.15.3c, and defined specifications for the system. In this thesis, we first design an OFDM receiver for the IEEE802.15.3c system. Specifically, we focus on the inner receiver which includes frame detection, carrier frequency offset estimation/compensation, channel estimation, and residual phase error tracking/compensation. Simulations show that the proposed receiver can meet the requirements defined in IEEE802.15.3c specifications.

Since the system operated in the 60GHz band endures a severe propagation loss.

In real-world implementation, a planar antenna array conducting beamforming is usually adopted to compensate for the loss. We consider two beamforming techniques, analog and hybrid, and propose a SDMA system for IEEE802.15.3c WPAN. The hybrid beamformer, which is developed recently, has the capability to null the interference from other users, but its implementation cost is higher. We then modeled the SDMA system as MIMO system, and design the corresponding detector. Simulations show that for a two-user system, if the separation of the pointing directions is larger than 15 degrees, satisfactory performance can be obtained. Although the hybrid beamformer can completely null the interference, its attenuation in the main beam is also large. It turns out that its performance is worse than that of analog beamforming.



7.2 Future work

As mentioned, the hybrid beamformer proposed recently null the interference completely. It turns out that this is not the best policy for the beamformer. As known, the performance of a communication system is determined by the SINR observed at the receiver. Thus, it is apparent that the hybrid beamformer should maximize the SINR when deriving its digital weights. By this way, good performance can be expected. In the thesis, we assume that the pointing directions of the array are known as a priori. In real-world, they are not. How to conduct the estimation fast and accurately deserves further research.

Reference

- [1] IEEE Std 802.15.3-2003, Part 15.3: Wireless Medium Access Control (MAC) and Physical Layer (PHY) Specifications for High Rate Wireless Personal Area Networks (WPANs), Nov, 2008.
- [2] Akita. K, Sakata. R, and Sato. K, "A phase compensation scheme using feedback control for IEEE 802.11a receiver" *Vehicular Technology Conference, 2004. VTC2004-Fall. 2004 IEEE 60th*
- [3] Z. Zhang, M. F. Iskander, Z. Yun, and A. H. Madsen, "Hybrid smart antenna system using directional elements—Performance analysis in flat rayleigh fading, " *IEEE Trans. Antennas Propag.*, vol. 51, no. 10, pp.2926 – 2935, Oct. 2003.
- [4] M. Rezk, W. Kim, Z. Yun, M. F. Iskander, "Performance comparison of a novel hybrid smart antenna systems versus the fully adaptive and switched beam antenna arrays," *IEEE Antennas and Wireless Propagation Letters*, vol.4, pp.285-288, 2005.
- [5] N. Celik, W. Kim, M. F. Demirkol, M. F. Iskander, "Implementation and experimental verification of hybrid beamforming" ,Oct. 2006.
- [6] Sau-Hsuan Wu, Lin-Kai Chiu, Ko-Yen Lin, and Shyh-Jong Chung . (2008). "Planar arrays hybrid beamforming for SDMA in millimeter wave applications". *Personal, Indoor and Mobile Radio Communications, 2008. PIMRC 2008. IEEE 19th International Symposium on*.
- [7] T. Kuhwald and H. Boche, "A constrained beam forming algorithm for 2D planar antenna arrays," in *Proc. IEEE VTC-Fall*. Amsterdam, The Netherlands, Sep. 1999.
- [8] W Zhao, GB Giannakis, "Sphere decoding algorithms with improved radius search", *IEEE Trans. on Commun.*, vol. 53, no. 7, pp. 1104- 1109,Jul. 2005.
- [9] J. Jalden and B. Ottersten, "On the complexity of sphere decoding in digital communications," *IEEE Trans. Signal Processing*, vol. 53, no. 4, pp. 1474–1484, Apr. 2005.

- [10] B. Steingrimsson, Z.Q. Luo and K.M. Wong, "Soft Quasi-Maximum-Likelihood Detection for Multiple Antenna Channels," accepted for publication in the *IEEE Tran. on Signal Processing*, 2003.
- [11] W. van Etten, "Maximum likelihood receiver for multiple channel transmission systems," *IEEE Trans. Commun.*, vol. 24, no. 2, pp. 276–283, Feb. 1976.
- [12] H. Sung, K. B. E. Lee, and J. W. Kang, "A simplified maximum likelihood detection scheme for MIMO systems," in *Proc.IEEE Vehicular Tech. Conf.*, vol. 1, Oct. 2003, pp. 419–423.

